Comparison of Global Climatic Responses to Large Tropical Volcanic Eruptions over the Last Millennium in Paleoclimatic Reconstructions and Model Simulations

ZHAOXIANGRUI HE,[a] ERNESTO TEJEDOR,[b] JASON E. SMERDON,[c,d] MATHIAS VUILLE,[a] LORENZO M. POLVANI,[d,e] RICHARD SEAGER,[d] AND IBUKI SUGIURA[d,f]

[a] *Department of Atmospheric and Environmental Sciences, University at Albany, State University of New York, Albany, New York*
[b] *Department of Geology, National Museum of Natural Sciences-Spanish National Research Council (MNCN-CSIC), Madrid, Spain*
[c] *Columbia Climate School, Columbia University, New York, New York*
[d] *Lamont-Doherty Earth Observatory, Columbia University, Palisades, New York*
[e] *Department of Applied Physics and Applied Mathematics, Columbia University, New York, New York*
[f] *Department of Earth and Environmental Sciences, Columbia University, New York, New York*

(Manuscript received 31 March 2025, in final form 10 December 2025, accepted 7 January 2026)

ABSTRACT: Large volcanic eruptions are known to significantly impact global climate for several years, yet a comprehensive comparison across the growing number of paleoclimate datasets has not been performed. Here, we assess the impacts of major eruptions over the Last Millennium on surface air temperature (SAT), Palmer drought severity index (PDSI), and 500-hPa geopotential height using tree-ring reconstructions, nine data assimilation (DA) products, and two climate model ensembles. We confirm robust global SAT cooling but find large differences in magnitude and persistence: Reconstructions based on tree-ring density show shorter, physically consistent cooling, whereas products dominated by tree-ring widths show longer persistence, likely reflecting biological memory. PDSI responses reveal coherent wetting over the western United States, the Mediterranean Basin, and southern South America, and coherent drying over northern and European Russia, central Asia, and southern Siberia, with divergence elsewhere. El Niño–Southern Oscillation responses differ across products, suggesting that any volcanically forced signal is weak relative to internal variability and highly sensitive to the background climate state. Geopotential height anomalies reveal widespread posteruption tropospheric contraction and robust extratropical circulation shifts, including negative height anomalies over mid- to high latitudes and wave-like patterns in the Southern Hemisphere. These anomalies are dynamically consistent with the spatial patterns of wetting and drying in PDSI, suggesting that volcanic forcing reorganizes large-scale atmospheric circulation in ways that influence hydroclimate. Together, these findings provide a comprehensive framework for interpreting volcanic impacts, strengthen confidence in regions with robust signals, and identify priority areas—particularly in the tropics and the Southern Hemisphere—where additional proxy coverage could reduce current uncertainties.

SIGNIFICANCE STATEMENT: This study presents the first comprehensive intercomparison of volcanic impacts on temperature, hydroclimate, and atmospheric circulation from tree-ring reconstructions, data assimilation products, and climate model ensembles. Reconstructions based on tree-ring density are the physically most consistent benchmark, showing shorter and more realistic duration of cooling, whereas products dominated by tree-ring widths overestimate persistence resulting from biological memory. Hydroclimate responses reflect coherent wetting in the western United States, the Mediterranean, and southern South America, and coherent drying in northern and European Russia, central Asia, and southern Siberia, with minimal agreement elsewhere. Responses of the El Niño–Southern Oscillation phenomenon remain inconsistent between products. We also connect hydroclimate signals with posteruption atmospheric height anomalies and associated extratropical circulation changes to provide a clearer framework for interpreting how volcanoes impact interactions between the ocean and atmosphere. This linkage also helps pinpoint priority regions—especially across the tropics and the Southern Hemisphere—where expanded, high-resolution proxy records could most effectively narrow current uncertainties.

KEYWORDS: Volcanoes; Drought; ENSO; Paleoclimate; Temperature; Data assimilation

1. Introduction

The Intergovernmental Panel on Climate Change (IPCC) Sixth Assessment Report (AR6) identifies volcanic forcing as the dominant driver of forced variability in surface air temperature over the last 2500 years (IPCC 2021). Volcanic aerosols are a natural driver of climate variability on interannual time scales, the effects of which are greatest within the first 2–5 years after a strong eruption. The AR6 also mentions that at least one large volcanic eruption is likely to occur in this century based on the distribution of volcanic eruptions over the last two millennia (IPCC 2021). However, the influences of volcanic eruptions on global temperature, monsoons, and El Niño–Southern Oscillation (ENSO) are poorly understood (Stoffel et al. 2024). A better understanding of volcanic impacts on climate is therefore critical for interpreting past climate, as well as enhancing our preparedness and resilience during future events. Moreover, intercomparisons of volcanic responses estimated from large-scale reconstructions and climate models provide insights into reconstruction and

Denotes content that is immediately available upon publication as open access.

Corresponding authors: Ernesto Tejedor, ernesto.tejedor@mncn.csic.es; Mathias Vuille, mvuille@albany.edu

DOI: 10.1175/JCLI-D-25-0179.1

model uncertainties, the former of which is dependent on proxy networks and reconstruction methodologies, while the latter depends on the forcing estimates and structural composition across the ensemble of available climate models (e.g., Anchukaitis and Smerdon 2022).

Previous studies have predominantly used three types of climate information to study the response of past climate to volcanic eruptions. The first type is proxy reconstructions, particular those derived from tree-ring networks. Early work by Briffa et al. (1998) used a Northern Hemisphere (NH) tree-ring density network spanning the last 600 years to estimate the effect of large volcanic eruptions on NH summer temperatures. Several large eruptions in the tree-ring-derived reconstruction were identified, such as the eruption of Huaynaputina, Peru, in 1600, and Kuwae, the southwestern Pacific, in 1452. Stoffel et al. (2015) later derived a NH summer temperature reconstruction over the past 1500 years using combined tree-ring width (TRW) and maximum latewood density (MXD) records to estimate the volcanic-induced cooling in the NH. They found a mean cooling anomaly over the land in the extratropical NH to be 0.8°–1.3°C. Schneider et al. (2015, 2017) similarly reconstructed NH summer temperatures, this time targeting the NH extratropics and exclusively using MXD data from 15 chronologies. They documented 14 cooling events in response to large volcanic eruptions during the Last Millennium, which agree well with records from polar ice cores in both hemispheres. The study estimated an average cooling response of 0.60°C ± 0.13°C to the 10 major events in the reconstruction.

Despite the successes of the studies highlighted above, the signals of volcanic eruptions in the TRW and MXD data show some discrepancies. D'Arrigo et al. (1992) compared the reconstructed temperature from TRW and MXD in northern Canada and found that the MXD chronologies match the time series of growing-season temperature better than TRW chronologies. Jones et al. (1995) found that the years of extremely low MXD match the volcanic events well and occur in North America and Europe coherently, while results based on TRW data exhibit less spatial coherence. D'Arrigo et al. (2013), Esper et al. (2015), and Schneider et al. (2015) compared the temperature responses to volcanic forcing in the TRW and MXD data and showed that the responses are weaker and more prolonged in TRW data than in MXD data. They suggested that the difference in biological memory of the data might cause such discrepancies. Lücke et al. (2019) conducted pseudoproxy experiments to show that biological persistence contributes to the dampening and prolonged response in temperature reconstructions based on TRW. In addition to tree-ring networks, coral records also have been used to investigate ENSO responses to volcanic forcing over the Last Millennium, and they consistently indicate an absence of a robust, systematic ENSO signal (Dee et al. 2020). In addition to temperature, tree-ring records are widely used to reconstruct past hydroclimate conditions, such as the Palmer drought severity index (PDSI) (Cook et al. 2004). The resulting spatially continuous, long-term drought atlases [e.g., the North American Drought Atlas, version 2 (NADAv2)] are based on the principle that the TRW of moisture-sensitive species is highly correlated with local soil moisture availability. These hydroclimate reconstructions offer crucial complementary information to temperature-based records, providing a proxy-based perspective on the response of the hydrologic cycle to external forcings like volcanic eruptions.

Earth system model simulations, particularly forced-transient simulations of the Last Millennium or longer, are the second type of information that has been widely used to evaluate volcanic impacts on climate (e.g., Maher et al. 2015; Stevenson et al. 2016; Gao and Gao 2018; Otto-Bliesner et al. 2016; Zanchettin et al. 2016). For instance, Man et al. (2014) examined the Last Millennium simulations performed with the Max Planck Institute Earth System Model (MPI-ESM; Giorgetta et al. 2013). Their findings indicate that the NH experiences greater cooling following large volcanic eruptions than the Southern Hemisphere (SH) and that the cooling occurs more strongly across continents than over oceans. Moreover, Ohba et al. (2013), Maher et al. (2015), Pausata et al. (2015), Stevenson et al. (2016), and Khodri et al. (2017) identified El Niño–like temperature and hydroclimate responses to large tropical and NH volcanic eruptions 1 year after the eruptions in climate model simulations, which is consistent with earlier studies based on paleoclimatic records (e.g., Adams et al. 2003; McGregor et al. 2010). The abovementioned model studies all showed that the El Niño–like responses might be due to a weakening of the trade winds over the western and central equatorial Pacific, although they proposed different mechanisms underlying the weakening. Predybaylo et al. (2017) employed a climate model to study how ENSO responses to Pinatubo-like volcanic forcing depend on the initial phase of ENSO in the eruption year. They found El Niño–like responses the year after the eruption for initial central or eastern Pacific El Niño and neutral phases but not for the initial La Niña conditions. Additionally, Iles and Hegerl (2014) showed that global monsoon rainfall decreases following volcanic eruptions in both observations and Coupled Model Intercomparison Project phase 5 (CMIP5) historical simulations and, in models, shifts away from the hemisphere with greater aerosol concentration. Colose et al. (2016) used simulations of two models to show that the intertropical convergence zone (ITCZ) shifts away from the hemisphere with greater volcanic forcing. Zuo et al. (2019) reported that the precipitation over the NH or SH monsoon regions is reduced following the volcanic eruptions in the same hemisphere but is enhanced after the volcanic eruptions in the other hemisphere. Recently, Zhou et al. (2024) analyzed simulations from the Paleoclimate Modelling Intercomparison Project phase 3 (PMIP3) and phase 4 (PMIP4) to show significant 2-yr wetting over drylands (i.e., regions where the annual potential evapotranspiration greatly exceeds annual precipitation) as a response to large tropical volcanic eruptions during the Last Millennium.

Data assimilation (DA) products are the third type of climate information that has been used to study the influences of volcanic forcing on climate. DA products combine proxy data and climate model simulations to obtain reconstructed estimates of multiple state variables, including gridded temperature, atmospheric pressure, and hydroclimatic fields, as well as

various dynamic ocean indices (see Smerdon et al. 2023 for a review). These DA techniques are broadly categorized as offline or online. Offline DA products [e.g., Paleo Hydrodynamics Data Assimilation (PHYDA), Last Millennium Reanalysis (LMR) v2.1; Zhu et al. 2020] use model simulations as a precomputed background field against which proxies are assimilated after the model run. Online DA (e.g., LMROnline) incorporates the proxy information into the model's state during the simulation, allowing the reconstructed climate state to dynamically influence the model's future evolution. This methodological difference contributes to the structural uncertainty across DA-based reconstructions. Zhu et al. (2020) used an offline ensemble DA approach to examine why paleoclimate reconstructions and climate model simulations differ in the magnitude and duration of volcanic cooling. They suggested that the sparse spatial coverage and seasonality biases of tree-ring records contribute to the weakened large-scale cooling seen in DA-based reconstructions relative to GCM simulations. Tejedor et al. (2021a) investigated global temperature responses to tropical volcanic eruptions in the PHYDA (Steiger et al. 2018) and LMR (Tardif et al. 2019) products, as well as model simulations from the Community Earth System Model, version 1 (CESM1), Last Millennium Ensemble (LME; Otto-Bliesner et al. 2016). They showed that the NH cooling caused by volcanic forcing lasts several years longer in the PHYDA and LMR than in the CESM1-LME, while the NH cooling in the PHYDA and LMR lasts 1 year longer and is 0.1°–0.2°C weaker than the NH MXD data. In a separate study, Tejedor et al. (2021b) examined global hydroclimatic responses to tropical volcanic eruptions in tree-ring reconstructions, PHYDA, and CESM1-LME. They showed that hydroclimatic responses in many regions are stronger and more persistent in PHYDA and tree-ring-based drought atlases than in CESM1-LME. King et al. (2021) produced 10 reconstructions of Northern Hemispheric near-surface temperature over the Last Millennium by using 10 different climate models to assimilate the Northern Hemisphere Tree-Ring Network Development (N-TREND; Wilson et al. 2016) data and found substantial differences in the spatial patterns and magnitudes of NH temperature responses to volcanic eruptions between the ensemble mean of their reconstructions and the other five paleo-temperature products. Paleoclimate DA was also used to show a weak relationship between volcanism and ENSO over the Last Millennium, which is inconsistent with climate models (Dee and Steiger 2022; Zhu et al. 2022). These studies emphasized the need for a paleoclimate reconstruction intercomparison framework to systematically evaluate how characteristics of proxy networks and reconstruction methodologies influence paleoclimate reconstructions.

Overall, previous studies have compared proxy reconstructions with individual DA products or with climate model ensembles to evaluate volcanic impacts on temperature and hydroclimate (e.g., Anchukaitis et al. 2017; Zhu et al. 2020; Dee and Steiger 2022; Tejedor et al. 2021a,b), but a systematic comparison across the growing collection of paleo-reconstructions, including multiple DA products, has not been conducted. Our study advances this line of research by systematically combining multiple tree-ring reconstructions, nine DA products, and two large model ensembles within a single framework. This integrated approach allows for a more rigorous assessment of where datasets agree, where they diverge, and how network composition and assimilation methodology influence the reconstructed climate signal in response to volcanic eruptions.

2. Data and methods

a. Datasets

In this study, we analyze reconstructions of surface air temperature (SAT) and PDSI from tree-ring networks, DA products, and model simulations to study the impacts of large tropical volcanic eruptions on global climate over the Last Millennium. The employed datasets are summarized in Tables 1–3 and are further described below.

We use four reconstructions of boreal summer SAT based on proxy data: the NH-MXD reconstruction (Schneider et al. 2015), the N-TREND reconstruction (Wilson et al. 2016), the reconstructions from Guillet et al. (2017), and those from Büntgen et al. (2021). The detailed information on these SAT reconstructions is summarized in Table 1. Additionally, we use several reconstructions of summer PDSI or self-calibrating PDSI (scPDSI) based on tree-ring data: the NADAv2 (Cook et al. 2004), the eastern Australia and New Zealand Drought Atlas (ANZDA; Palmer et al. 2015), the Mexican Drought Atlas (MXDA; Stahle et al. 2016), the South American Drought Atlas (SADA; Morales et al. 2020), and the Greater Eurasian Drought Atlas (GEDA) (Cook et al. 2024). These PDSI and scPDSI reconstructions (drought atlases) are summarized in Table 2, all of which were standardized over the 1500–1850 CE interval.

Data assimilation techniques statistically combine the climate signals in paleoclimate records (e.g., tree rings, corals, ice cores, lake cores, etc.) with the dynamical constraints provided by climate models to produce spatially continuous climate field reconstructions with estimates of uncertainty (e.g., van der Schrier and Barkmeijer 2005; Bhend et al. 2012; Goosse et al. 2010). The following nine DA products are analyzed herein: the LMR, version 2.1 (LMR v2.1; Tardif et al. 2019), PHYDA (Steiger et al. 2018), LMROnline (Perkins and Hakim 2017), Ensemble Kalman Fitting Paleo-Reanalysis, version 2.0 (EKF400 v2.0; Franke et al. 2020; Valler et al. 2022), PaleoSST (Samakinwa et al. 2021), and Modern Era Reanalysis (ModE-RA; Valler et al. 2023, 2024), as well as those created by Neukom et al. (2019), Zhu et al. (2020), and King et al. (2021). An online approach using a time-dependent prior from a linear inverse model of coupled atmosphere–ocean dynamics was used to produce LMROnline (Perkins and Hakim 2017); the offline ensemble square root filter (EnSRF) DA approach was used to create King et al. (2021) and ModE-RA; and the offline ensemble Kalman filter (EnKF) DA approach was used to generate the PHYDA (Steiger et al. 2018). The LMR (Tardif et al. 2019) and the DA products of Zhu et al. (2020, 2022) use the EnSRF for assimilation, following the approach of Whitaker and Hamill (2002) as explicitly stated in Tardif et al. (2019). An important distinction across DA products is how the climate model prior (or background field) is employed. Some

TABLE 1. Employed reconstructions of boreal summer SAT from proxy networks.

Name (reference) and source	Region	Period (CE)	Chronology type
Büntgen et al. (2021) https://www.ncei.noaa.gov/access/paleo-search/study/33215	NH (30°–90°N)	1–2016	TRW
Guillet et al. (2017) https://www.ncei.noaa.gov/access/paleo-search/study/21090	NH (40°–90°N)	500–2000	TRW and MXD
NH-MXD (Schneider et al. 2015) https://www.ncei.noaa.gov/access/paleo-search/study/18875	NH (30°–90°N)	600–2002	MXD
N-TREND (Wilson et al. 2016; Anchukaitis et al. 2017) https://www.ncei.noaa.gov/access/paleo-search/study/19743	NH (40°–75°N)	750–2014	TRW and MXD

DA frameworks (e.g., LMR v2.1) sample the prior ensemble from the full simulation period, which ensures the prior at any given time is independent of the specific climate forcing for that year. This independence is crucial as it means the assimilated product is constrained by the proxy data against a purely model-forced background. Other approaches may restrict the prior ensemble to the year being reconstructed (or a narrow time window), which can lead to the assimilated product being potentially more reflective of the modeled volcanic forcing response if the model ensemble is not large enough to span the internal variability. Given the high sensitivity of the volcanic response to the pre-eruption state, this difference in prior sampling can be a significant contributor to the differences in the magnitude and persistence of the volcanic signal across the various DA products. More information can be found in Table 3. It is important to note that Modern Era Simulations (ModE-Sim), which provides the prior for ModE-RA, is an atmosphere-only model ensemble forced with prescribed sea surface temperature (SST) and sea ice reconstructions. Variability in tropical SSTs, including ENSO, is therefore externally specified rather than generated dynamically. As a result, ENSO responses in ModE-Sim and ModE-RA are partially dependent on the employed SST reconstructions and cannot be considered fully independent of other proxy-based SST reconstructions. PaleoSST is included here only as an independent reconstruction product for comparison, not as input to the DA products or model priors.

We also analyze two ensembles of model simulations: the CESM1-LME (Otto-Bliesner et al. 2016), from which we use 10 fully coupled simulations with all forcings (including solar, volcanic, land use, greenhouse gas, orbital, and ozone–aerosol forcings) spanning the period 850–2006 CE, and the fully coupled ModE-Sim (Valler et al. 2022) with all forcings that span the period 1420–2009 CE (with 60 ensemble members for 1420–1850 and 36 ensemble members for 1850–2009). The CESM1 and ECHAM6 (the atmospheric general circulation component of the Max Planck Institute Earth System Model) models were used to create the CESM1-LME and ModE-Sim, which were in turn used as priors for the PHYDA and ModE-RA DA products, respectively. The CESM1 is also the successor of the Community Climate System Model, version 4 (CCSM4), which was used as the prior for the LMR v2.1, Zhu et al. (2020), and LMROnline products. The ECHAM6 is the successor of ECHAM5.4, which is the model used to develop the prior of EKF400 v2.0.

b. *Event selection and superposed epoch analysis*

To investigate the impacts of volcanic eruptions on climate, we first selected the large tropical volcanic events between 850 and 1850 CE. Our criterion for choosing such large volcanic events follows that of Tejedor et al. (2021a,b), who analyzed tropical events with volcanic stratospheric sulfur injection (VSSI) or stratospheric sulfate aerosol injection (SSAI) exceeding those of the 1991 Mount Pinatubo eruption (i.e., VSSI $>$ 8.78 Tg S or SSAI $>$ 30.1 Tg). For all of the proxy reconstructions, DA products, and the ModE-Sim, we identified events using the VSSI data from the eVolv2k_v3 dataset (Toohey and Sigl 2017, 2019), which reconstructs volcanic forcing from 500 BCE to 1900 CE using ice-core records from Greenland and Antarctica. For the CESM1-LME, we identified events using the SSAI data from the ice-core volcanic index 2 (IVI2; Gao et al. 2008) dataset, which also employs Greenland and Antarctica ice-core records to reconstruct past volcanic forcing over the period 500–2000 CE. The IVI2 data were used to select the volcanic events in

TABLE 2. Employed gridded reconstructions of summer PDSI from proxy networks.

Name (reference) and source	Region	Period (CE)	Chronology type
ANZDA (Palmer et al. 2015) https://www.ncei.noaa.gov/access/paleo-search/study/20245	Eastern Australia and New Zealand	1500–2012	TRW
GEDA (Cook et al. 2024) http://drought.memphis.edu/GEDA/	Eurasia	1000–2020	TRW
MXDA (Stahle et al. 2016) https://www.ncei.noaa.gov/access/paleo-search/study/20353	Mexico	1400–2012	TRW
NADAv2 (Cook et al. 2004) https://www.ncei.noaa.gov/access/paleo-search/study/6319	North America	800–2005	TRW
SADA (Morales et al. 2020) https://www.ncei.noaa.gov/access/metadata/landing-page/bin/iso?id=noaa-recon-30612	Southern South America	1400–2000	TRW

TABLE 3. Employed DA products.

Name (reference) and source	Region	Period (CE)	Prior	Assimilated proxy network
EKF400 v2.0 (Franke et al. 2020; Valler et al. 2022) https://doi.org/10.26050/WDCC/EKF400_v2.0	Global	1603–2003	ECHAM5.4	TRW, MXD, ice cores, documentary data
King et al. (2021) https://doi.org/10.5281/zenodo.3989940	NH (30°–90°N)	750–2011	10 CMIP5 models	NTREND (TRW, MXD)
LMR v2.1 (Tardif et al. 2019) https://www.ncei.noaa.gov/access/paleo-search/study/27850	Global	0–2000	CCSM4	TRW, MXD, corals, ice cores
LMROnline (Perkins and Hakim 2017) https://doi.org/10.5281/zenodo.4626197	Global	1000–2000	CCSM4 and MPI-ESM	TRW, MXD, corals, ice cores
Neukom et al. (2019) https://www.ncei.noaa.gov/access/paleo-search/study/26850	Global	1–2000	CESM1-LME	PAGES2k proxy network (TRW, MXD, corals, speleothems, ice cores)
ModE-RA (Valler et al. 2023, 2024) https://doi.org/10.26050/WDCC/ModE-RA_s14203-18501	Global	1421–2008	ModE-Sim	Early instrumental data, PAGES2k, OCEAN2k, ISO2k, NTREND
PHYDA (Steiger et al. 2018) https://www.ncei.noaa.gov/access/paleo-search/study/24230	Global	0–2000	CESM1-LME	TRW, MXD, corals, ice cores, speleothems, Lake sediment records
PaleoSST (Samakinwa et al. 2021) https://doi.org/10.6084/m9.figshare.c.5369309.v1	Global ocean	1000–1849	Neukom et al. (2019)	Marine proxies (corals, foraminifera, alkenones)
Zhu et al. (2020) https://doi.org/10.5281/zenodo.3725030	Global	0–2000	CCSM4	Version with TRW only

CESM1-LME because the IVI2 data served as the volcanic forcing in the simulations. We defined tropical volcanic eruptions in the eVolv2k_v3 dataset as those that occurred within the range of 25°S–25°N. Because locations are not explicitly provided in the IVI2 data, tropical eruptions were defined as those with SSAI values greater than zero in both the Northern and Southern Hemispheres, as tropical volcanic eruptions are expected to affect both hemispheres.

To analyze the climate responses to large volcanic forcing, we employed superposed epoch analysis (SEA; Hegerl et al. 2003). This involves first calculating the anomalies of climatic variables (e.g., SAT and PDSI) for the 20 years after a volcanic event, relative to the 5-yr average prior to the event. Results based on anomalies with respect to either a 5-yr or 10-yr average prior to volcanic eruptions (a common baseline in many other studies) were found to be very similar in most cases (not shown). We repeated this step for each of the selected volcanic events. When two volcanic events occur within 10 years, we treated them as "double events" and only select the second event, calculating anomalies relative to the 5-yr average before the first event (Tejedor et al. 2021a,b). Otherwise, the cooling peak of the first event in TRW data would appear several years after the eruption (e.g., 1453 Kuwae eruption as shown in Esper et al. 2015; Schneider et al. 2015). Finally, we averaged the anomalies of climate variables across the selected volcanic events. The years of the large tropical volcanic eruptions from 850 to 1850 CE identified using eVolv2k_v3 and IVI2 are shown in Table 4.

c. *Bootstrap hypothesis testing*

We used a bootstrap method to test the significance of the anomalies resulting from the SEA. Our null hypothesis for the SEA is that the difference between the responses to volcanic forcing and variations related to random internal variability is zero. To perform the bootstrap testing, we follow these steps: 1) We randomly selected 25 years from all the years within the entire analyzed interval to obtain a pseudoevent; 2) we computed the anomalies relative to the first 5 years of the pseudoevent using the SEA; 3) we repeated the first and second steps 10 000 times to obtain a distribution of climate responses to random forcing from 5 years prior to this forcing to 20 years afterward; and 4) we compared the climate response after actual volcanic events to the bootstrap-estimated distribution. If the volcanic response is stronger than 95% of the bootstrapped climate responses, it is considered significant at the 95% confidence level.

TABLE 4. The years of large tropical volcanic eruptions over the period 850–1850 CE from eVolv2k_v3 and IVI2. The years within parentheses are not analyzed because they are the first of two events that occurred within 10 years of each other (i.e., double events).

Name of volcanic forcing datasets (reference) and source	Years of large tropical volcanic eruptions
eVolv2k_v3 (Toohey and Sigl 2019) https://doi.org/10.26050/WDCC/eVolv2k_v3	1108, 1171, 1230, 1257, (1276), 1286, 1345, (1453), 1458, (1595), 1600, 1640, 1695, (1809), 1815, (1831), 1835
IVI2 (Gao et al. 2008) https://www.ncei.noaa.gov/access/paleo-search/study/8701	1167, 1227, 1258, (1275), 1284, 1341, 1452, 1600, 1641, (1809), 1815, 1835

3. Results

a. Surface air temperature responses to volcanic forcing

Previous studies (e.g., King et al. 2021; Tejedor et al. 2021a) used reconstructions based on tree-ring networks, DA products, and model simulations to investigate the responses of global temperature to large tropical volcanic eruptions over the Last Millennium. These studies consistently reported nearly global-scale cooling following such eruptions. In this section, we extend these findings by analyzing additional datasets (e.g., LMROnline and ModE-RA) to assess the impacts of past volcanic eruptions on global temperature. The spatial patterns of the surface temperature response derived by the SEA over the events listed in Table 4, averaged over the first three postevent years, are shown in Fig. 1. The results from all of the datasets reveal cooling globally, which is consistent with the expected effects of volcanic aerosols injected into the stratosphere. These aerosols reflect shortwave radiation back to space and hence reduce the shortwave radiation received at the surface, thereby cooling the lower troposphere. The cooling over land in the NH and over the Arctic Ocean is stronger than over the tropics and SH. This asymmetry may be due to the larger proportion of sulfur dioxide released into the atmosphere over the NH, relative to the SH, as evidenced by an average ratio between the NH and SH VSSI of 1.77 (2.00 for the SSAI). Another contributing factor may be the higher fraction of ocean in the SH, which provides more thermal buffering and reduces the temperature response relative to the NH (Cheng et al. 2022).

Additionally, the SAT responses over the eastern tropical Pacific exhibit contrasting patterns across datasets. In some, such as PHYDA, the responses are positive, whereas in others, such as Zhu et al. (2020), they are negative (Fig. 1). Previous studies suggested that volcanic events induce El Niño conditions (e.g., Adams et al. 2003; McGregor et al. 2010; Ohba et al. 2013; Maher et al. 2015; Pausata et al. 2015; Stevenson et al. 2016; Khodri et al. 2017; Predybaylo et al. 2017), and large eruptions (e.g., Mount Pinatubo 1991) could force the likelihood and amplitude of an El Niño event above internal variability (Emile-Geay et al. 2008). Yet others have suggested that La Niña conditions may be the forced response of volcanism (e.g., Wahl et al. 2014; Tejedor et al. 2021a,b). In contrast to studies that have argued for strong connections between volcanism and ENSO responses, Dee et al. (2020) and Dee and Steiger (2022) estimated a weak and statistically insignificant El Niño–like response to large tropical volcanic eruptions over the Last Millennium using coral reconstructions and the PHYDA. Moreover, Zhu et al. (2022) showed that there was a weak relationship between volcanism and ENSO over the Last Millennium by integrating coral and tree-ring proxies into a reconstruction of ENSO using paleoclimate data assimilation. Figure 2a shows the time series of SAT or SST anomalies in the Niño-3.4 region before and after volcanic eruptions. Here, the Niño-3.4 index is defined as the SAT or SST averaged over the equatorial central Pacific (5°S–5°N, 170°–120°W). The results from various datasets reveal substantial disagreement. For example, the Niño-3.4 anomalies from the PaleoSST are generally positive after the volcanic events, while the anomalies in Zhu et al. (2020) and EKF400 v2.0 are negative after the events. Additionally, Figs. 2b–d show the distributions of the Niño-3.4 index anomalies during the first 3 years after the eruptions. In some datasets (e.g., PHYDA; Neukom et al. 2019, and LMROnline), the Niño-3.4 anomalies tend to shift from positive to neutral, while in others (e.g., LMR v2.1 and Zhu et al. 2020), they transition from negative to neutral. These collective results indicate a lack of consensus on the ENSO response to volcanic forcing across the products analyzed and suggest that dataset uncertainties are likely the largest contributor to the broad disagreement in the literature about the effect of volcanic eruptions on ENSO. It is worth noting that Zhu et al. (2022), who assimilated both tree-ring and coral proxies, could provide a stronger constraint on tropical Pacific variability than Zhu et al. (2020), who assimilated only tree-ring data. Although we retained Zhu et al. (2020) for consistency within our common analysis period and variables across datasets, most other DA products included in this study (e.g., PHYDA, LMR v2.1, LMROnline) also assimilate corals, ensuring that our conclusions already reflect products with coral information. Future work should explicitly compare results with Zhu et al. (2022) to further test the robustness of ENSO-related findings.

The spatial patterns of SAT responses to volcanic forcing are compared in Fig. 3 using the level of agreement as the number of datasets that align in the sign of the response. The SAT responses from tree-ring reconstructions, DA products, and models generally agree with each other in sign over the continents in the NH (which is the region where the three types of temperature reconstructions overlap). This agreement suggests that different datasets generally reproduce the mid- and high-latitude NH cooling in response to volcanism. However, the warm anomalies over eastern Canada in N-TREND (Fig. 1a) contribute to disagreements over that region. Significant disagreements are also observed in the SAT responses over the equatorial Pacific, Southern Ocean, central Africa, and the Himalayas (Fig. 3c).

We subsequently examine the average responses of area-weighted mean global, NH, tropical, and SH SAT to large tropical volcanic forcing. During the first posteruption year, the global mean SAT anomaly ranges from −0.1° to −0.3°C across the nine reconstructions and DA products analyzed, averaged over the selected eruptions. The corresponding multidataset mean cooling is approximately −0.2°C. These values provide a quantitative baseline against which to interpret the temporal evolution of SAT responses shown in Fig. 4. The influence of volcanic forcing on NH SAT is notably larger than on tropical, SH, and global-mean SAT (Fig. 4). The SAT responses following volcanic eruptions are larger in the models (i.e., CESM1-LME and ModE-Sim) than in the DA products, except for the ModE-RA. Moreover, Fig. 4b shows that the magnitude of the NH SAT response in NH-MXD is consistent with those from PHYDA, Neukom et al. (2019), and King et al. (2021). The NH SAT responses seen in N-TREND, Guillet et al. (2017), and Büntgen et al. (2021) are more persistent than those in the DA products and model simulations. The responses from N-TREND and Guillet et al. (2017)

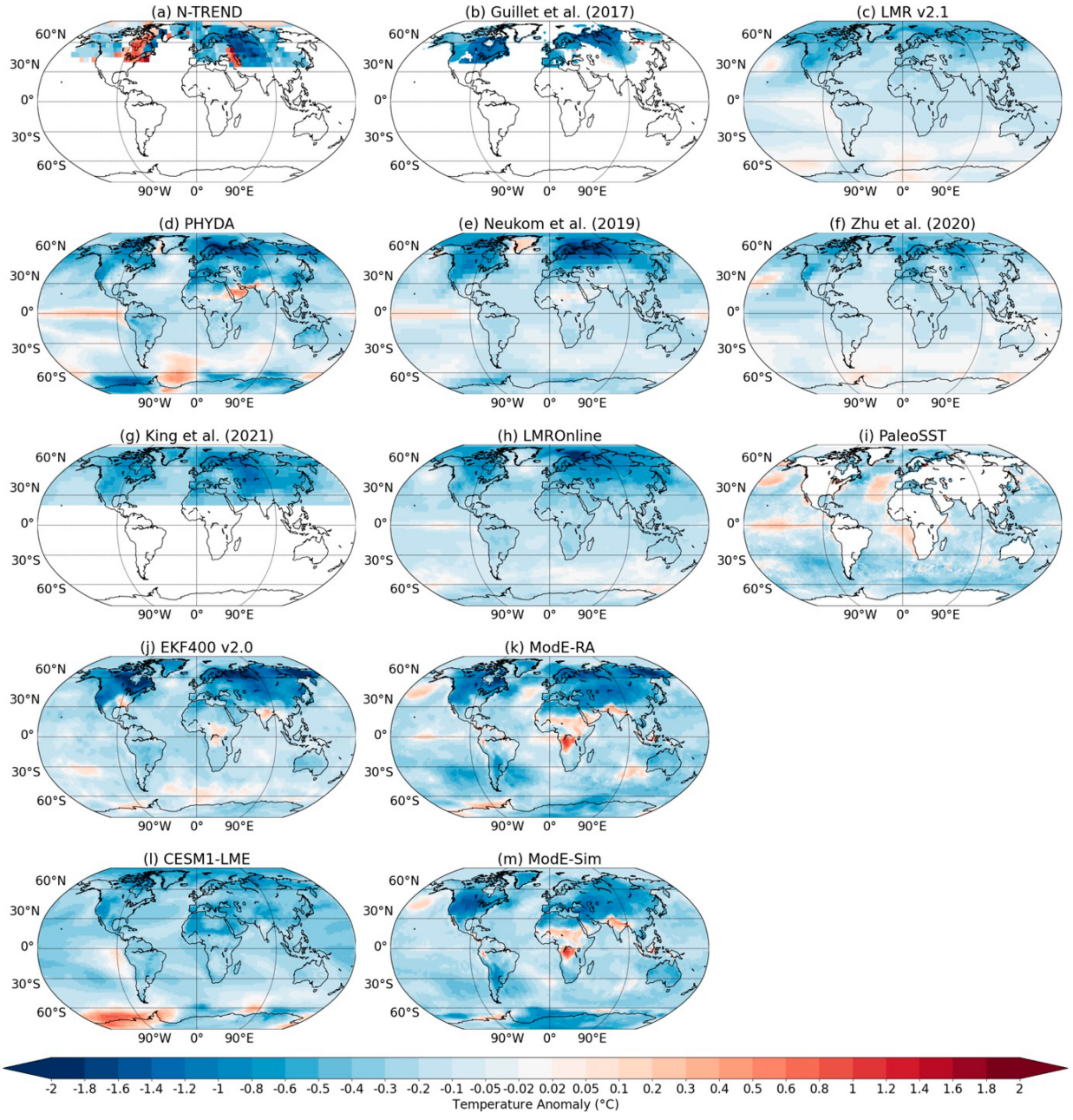

FIG. 1. The 3-yr averaged postvolcanic temperature anomalies relative to the five pre-eruption years for the large tropical volcanic eruptions over the period 850–1850 CE. The temperature anomalies from the (a) N-TREND, (b) Guillet et al. (2017), (c) LMR v2.1, (d) PHYDA, (e) Neukom et al. (2019), (f) Zhu et al. (2020), (g) King et al. (2021), (h) LMROnline, (i) PaleoSST, (j) EKF400 v2.0, (k) ModE-RA, (l) CESM1-LME, and (m) ModE-Sim. The panels (a) and (b) are from tree-ring reconstructions; the panels (c)–(k) are from DA products; the panels (l) and (m) are from model simulations. The values from N-TREND, Guillet et al. (2017), PHYDA, ModE-RA, CESM1-LME, and ModE-Sim represent JJA SAT anomalies in (a), (b), (d), and (k)–(m). The values from LMR v2.1, Neukom et al. (2019), Zhu et al. (2020), King et al. (2021), and LMROnline represent annual SAT anomalies in (c) and (e)–(h). The values from PaleoSST in (i) represent annual SST anomalies. The values from EKF400 v2.0, ModE-RA, and ModE-Sim represent the SAT responses to large tropical volcanic events over 1603–1850, 1421–1850, and 1420–1850 CE, respectively (for all the other datasets, 1000–1850 CE). All the results from DA products and model simulations are based on the ensemble mean of the datasets.

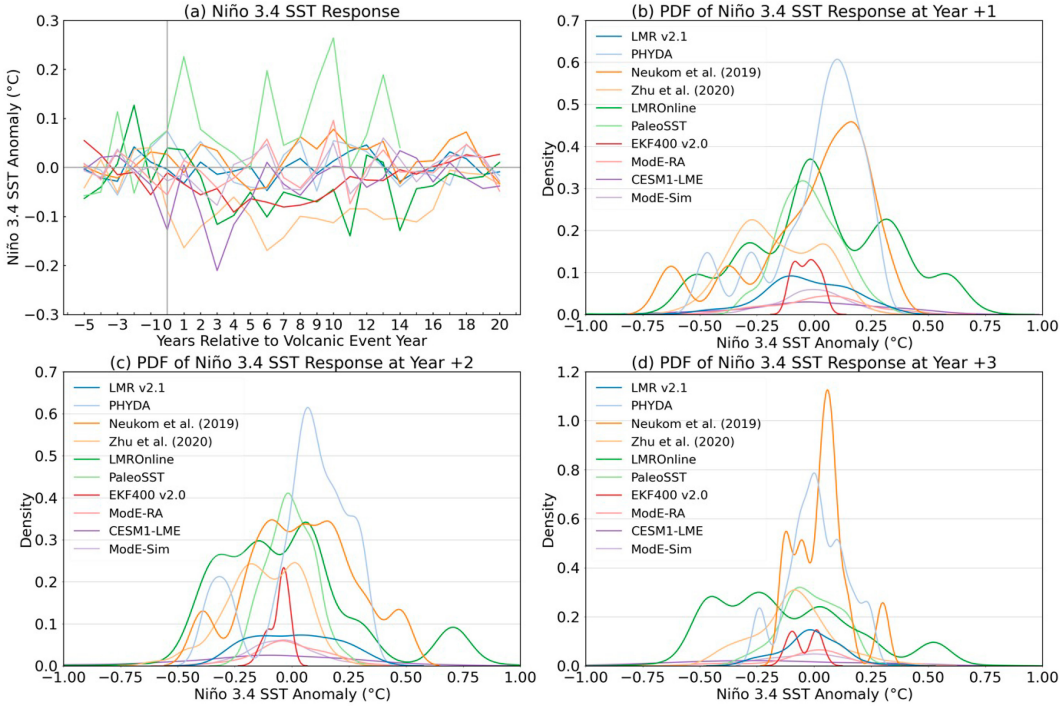

FIG. 2. (a) The Niño-3.4 SST anomalies relative to the average of the five pre-eruption years. The Niño-3.4 index is consistently defined across all datasets as the annual-mean SAT or SST averaged over the equatorial central Pacific (5°S–5°N, 170°–120°W), ensuring comparability. Probability density functions (PDFs) of the Niño-3.4 SST anomalies in the (b) first, (c) second, and (d) third years after the volcanic eruptions. PDFs are based on all ensemble members of each respective dataset.

are stronger than the DA or model estimates, although it should be noted that N-TREND and Guillet et al. (2017) represent SAT averages over different latitude ranges than the rest of the datasets. This is consistent with previous studies (e.g., D'Arrigo et al. 1992, 2013; Jones et al. 1995; Esper et al. 2015; Schneider et al. 2015; Lücke et al. 2019; Zhu et al. 2020; Tejedor et al. 2021a) that have indicated that MXD serves as a better proxy for surface temperature responses to volcanism than TRW (since NH-MXD was solely reconstructed from MXD data, while the other tree-ring networks were reconstructed wholly or partly from TRW). Figure 5 provides boxplots of the 3-yr averaged SAT responses to volcanic forcing. All datasets show a cooling signal after volcanic eruptions, with the largest responses over the NH. The results from the DA products and model simulations are generally consistent, although some differences are apparent between EKF400 v2.0, ModE-RA, ModE-Sim, and the other DA datasets (Fig. 5). These differences may nevertheless reflect the varying time periods analyzed (EKF400 v2.0 covers the period 1603–1850 CE, ModE-RA extends from 1421 to 1850 CE, and ModE-Sim represents 1420–1850 CE, while the rest of the datasets cover 850–1850 CE), resulting in a different number of volcanic events included in each SEA. Additionally, the result from NH-MXD is consistent with the results from the PHYDA, Neukom et al. (2019), King et al. (2021), and LMROnline datasets (Fig. 5b), supporting the results from PMIP3 and PMIP4 (i.e., the NH cooling due to volcanic eruptions is 0.1°–0.5°C) (IPCC 2021). The cooling signal seen in N-TREND, Guillet et al. (2017), and Büntgen et al. (2021) is stronger than in the DA products and model simulations (Fig. 5b), reinforcing the conclusion that MXD is a more reliable proxy for SAT than TRW.

Earlier studies (e.g., D'Arrigo et al. 2013; Esper et al. 2015; Schneider et al. 2015; Lücke et al. 2019; Zhu et al. 2020; Tejedor et al. 2021a) examined the persistence of the temperature response to volcanic eruptions from various datasets. The general results from these studies found that the persistence in MXD data is shorter than in TRW data, and the persistence in model simulations is shorter than in tree-ring networks and DA products. This difference is likely due to the biological memory of the TRW data (which were also assimilated into DA products and hence incorporated this persistence). We quantitatively examine the persistence of the SAT response to volcanic forcing across different datasets. We define persistence as the number of years following the event year for which the SAT response is significant at the 95% confidence level. Figure 6 shows that median persistence across products typically lies between 3 and 6 years globally (Fig. 6a), with longer tails (>10 years) for TRW-heavy products (N-TREND; King et al.) and LMROnline. Offline DA products (LMR v2.1 and PHYDA) and model ensembles show notably shorter persistence, generally recovering after ~5 years. In the Northern Hemisphere (Fig. 6b), the contrast is sharpest: NH-MXD (Schneider et al. 2017), CESM1-LME, and ModE-Sim exhibit recovery within 3–6 years, while

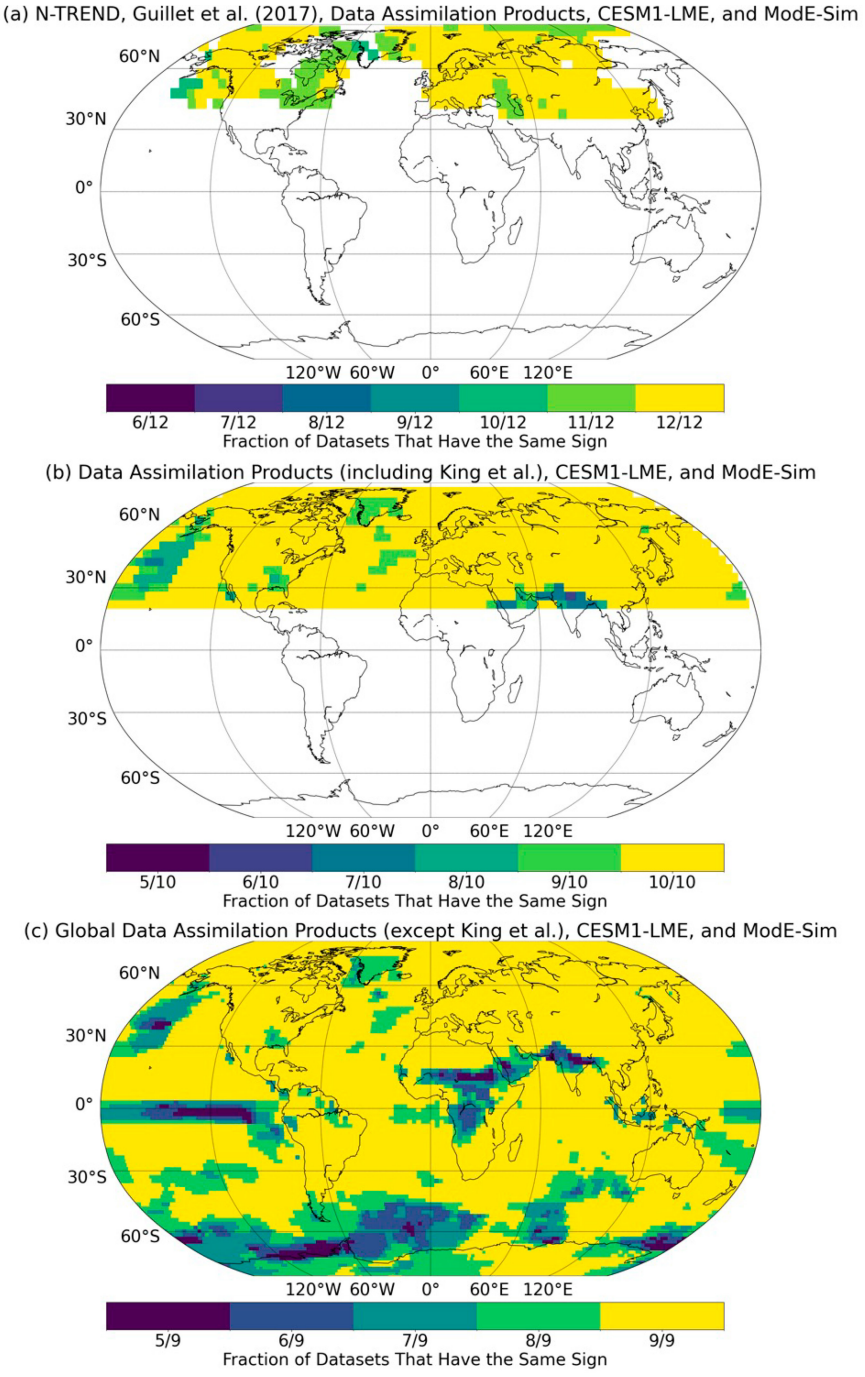

FIG. 3. The agreement in the signs of SAT responses among the datasets (except PaleoSST) in Fig. 1. The agreement among (a) the datasets shown in Fig. 1 over the land, (b) the data assimilation products and model simulations, and (c) the global data assimilation products (except King et al. 2021) and model simulations.

TRW-dominated reconstructions display persistence of >8 years, with upper tails extending to ~15–20 years. This highlights biological memory as a key source of prolonged cooling in TRW-based reconstructions.

Interestingly, the tropics (Fig. 6c) show slightly higher median persistence than the NH, with DA products (LMR v2.1, PHYDA) maintaining significant cooling for up to 8 years. However, this persistence occurs at a much lower amplitude compared to CESM1-LME and ModE-Sim (Fig. 4c), which display a stronger initial cooling but recover more quickly. One interpretation of this mismatch is that reconstructions may be underestimating the initial volcanic signal in the tropics, possibly

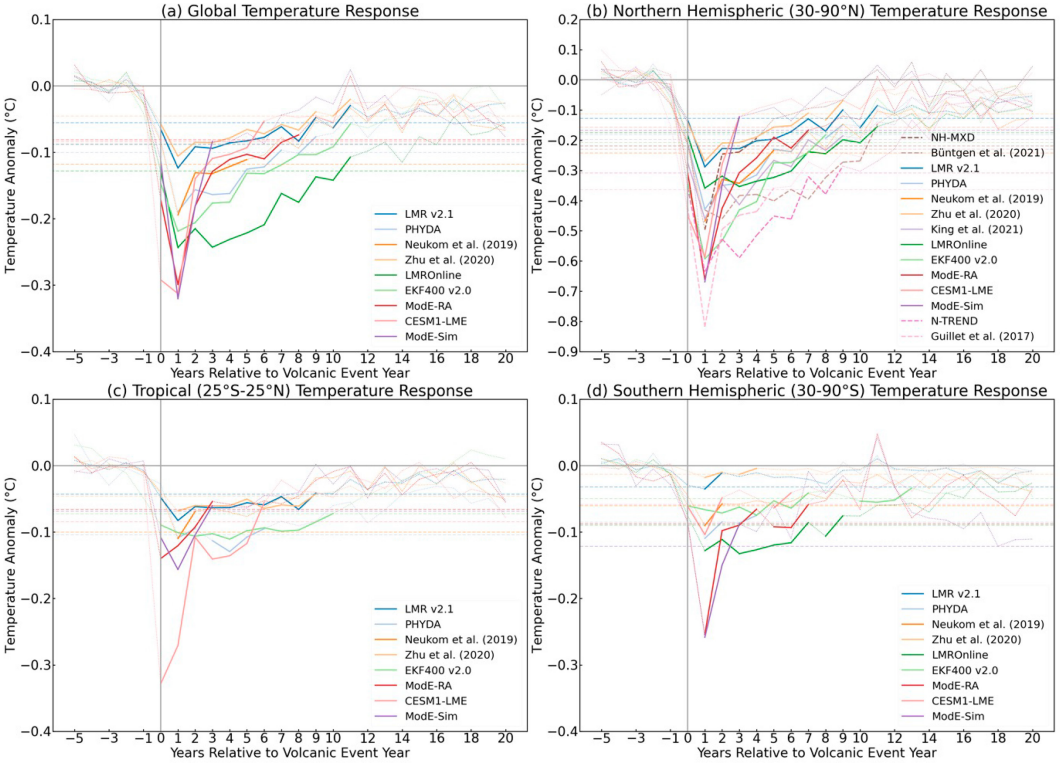

FIG. 4. The SAT responses to large tropical volcanic eruptions averaged over the (a) globe, (b) NH, (c) tropics, and (d) SH. The time series from the N-TREND and Guillet et al. (2017) represent SAT averaged over 40°–75°N and over 40°–90°N, respectively. The significant anomalies from tree-ring networks are shown in dashed lines, while the significant anomalies from DA products and model simulations are shown in solid lines. The insignificant anomalies are shown in dotted lines. The horizontal dashed lines indicate the significant thresholds at the 95% confidence level for each dataset, i.e., internal variability. Note that the scaling of the *y* axis differs in (b) compared to the other panels.

due to proxy network limitations or temporal smoothing, thereby extending the recovery artificially. Alternatively, it is also possible that models may overestimate the strength of the initial response or underestimate slower recovery processes, leading to a shorter simulated persistence. Overall, Fig. 6 confirms that volcanic cooling persistence varies widely across products, is typically longer in TRW-based networks, and shows no clear scaling with eruption magnitude.

In the SH (Fig. 6d), persistence is generally shortest (1–3 years), consistent with stronger ocean damping and a lower signal-to-noise ratio, though LMROnline again exhibits longer tails than its offline counterpart. Such weaker and less significant cooling is consistent with its larger ocean fraction and thermal inertia, which tend to dampen the immediate response while modestly prolonging recovery (Stenchikov et al. 2009; Zanchettin et al. 2013).

Together, Fig. 6 underscores that volcanic cooling persistence is highly product dependent, typically longer in TRW-based datasets and in the tropics, and shows no clear scaling with eruption magnitude.

b. Hydroclimate responses to volcanic forcing

Tejedor et al. (2021b) examined the PDSI responses to large tropical volcanic eruptions from drought atlases, PHYDA, and CESM1-LME and found that they were stronger and more persistent in PHYDA and tree-ring-based drought atlases than in the CESM1-LME. In this section, we extend this analysis by evaluating PDSI responses to large tropical volcanic forcing using a more comprehensive collection of reconstructions. The analysis period for the PDSI is shorter than that for SAT because the common interval of all datasets only covers the period 1500–1850 CE (Tables 2 and 3).

Figure 7 represents the SEA results that demonstrate the global PDSI responses to large tropical volcanic forcing during the first 3 years following the events. Dry conditions are observed over some tropical regions, such as West Africa and Indonesia, consistent with the precipitation responses reported by Zuo et al. (2019). Most panels in Fig. 7 (except Fig. 7l) show wetting over western North America and the Mediterranean basin. Despite these similarities, the global PDSI responses across datasets are inconsistent (e.g., eastern United States and southern South America), suggesting larger uncertainties in the hydroclimate response to volcanism relative to the SAT responses. The results from LMR v2.1 (Figs. 7d–f), which represent annual calendar-year PDSI anomalies, might contribute to these discrepancies. Villamayor et al. (2023) showed that, in two different PMIP4 model simulations, large volcanic eruptions in the tropics and the extratropical NH

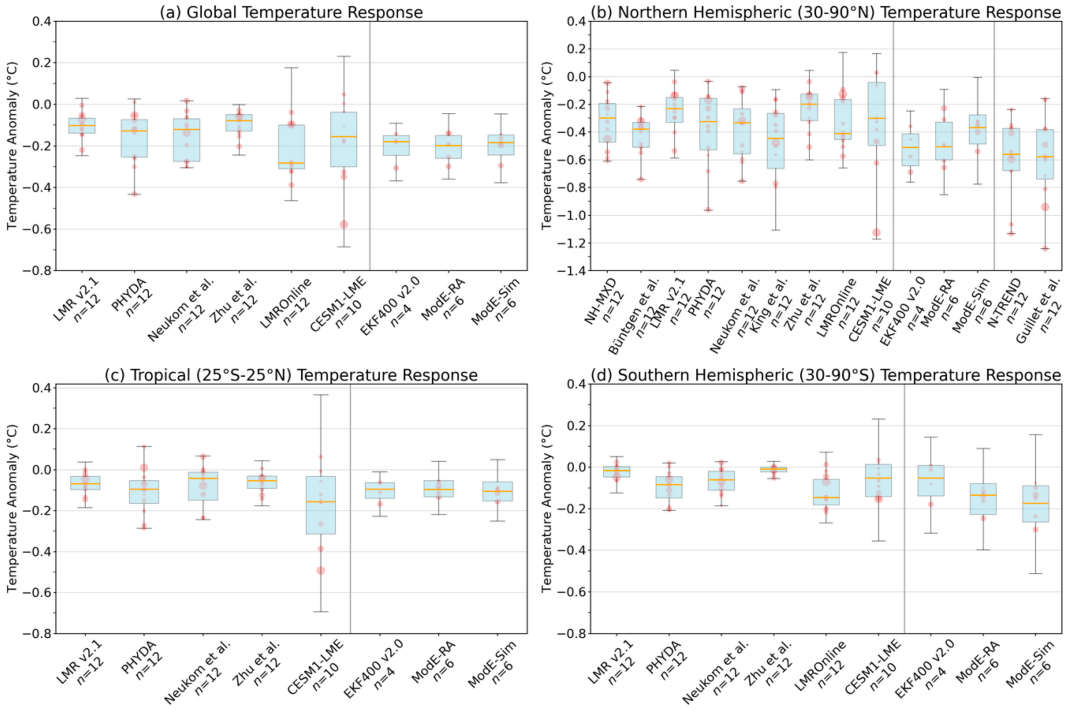

FIG. 5. The boxplots for the 3-yr averaged postvolcanic SAT responses to large tropical volcanic eruptions averaged over the (a) globe, (b) NH (30°–90°N), (c) tropics (25°S–25°N), and (d) SH (30°–90°S). The results from N-TREND represent the SAT anomalies averaged over 40°–75°N; the results from Guillet et al. (2017) represent the SAT anomalies averaged over 40°–90°N. The boxplots from the DA products and model simulations are based on all the ensemble members of the datasets, while the dots from the DA products and model simulations represent the ensemble means of responses to individual volcanic events in the datasets. The sizes of the dots correspond to the intensities (VSSI) of the volcanic eruptions (i.e., a larger dot corresponds to a stronger volcanic eruption, and the opposite is also true). Boxes range from the upper to the lower quartiles, whiskers indicate the 5th–95th percentiles, and the solid line is the median. Note that the scaling of the *y* axis differs in (b) compared to the other panels.

both cause drying over the West African Sahel region. However, tropical eruptions were found to reduce precipitation over the Congo basin, whereas extratropical NH eruptions increase precipitation there. Results from PHYDA and CESM1-LME (Figs. 7g–l) show drying over parts of West Africa, but this response is not evident in LMR v2.1 (Fig. 8d). Additionally, Zhou et al. (2024) found increases in both the PDSI and the standardized precipitation evapotranspiration index (SPEI) and declines in aridity as measured by the aridity index (AI) over most of the global drylands—including the southwestern United States, southeastern South America, northern and southern Africa, the Middle East, and Australia, (excluding West Africa)—in response to large tropical volcanic eruptions in models participating in PMIP3 and PMIP4. These findings are consistent with results from CESM1-LME but diverge from those of PHYDA and LMR v2.1 (Fig. 7). Overall, while some regional patterns are consistent across datasets, such as drying in certain tropical regions and wetting in western North America and the Mediterranean basin, there remains a notable lack of consensus on the global hydroclimate response to volcanic forcing. This underscores the need for further refinement of hydroclimate reconstructions and models.

Figure 8 shows the agreement among the datasets on the signs of the PDSI spatial patterns in Fig. 7. Areas where at least three out of four products agree (yellow-green shading) are limited, highlighting that robust posteruption hydroclimate responses are spatially confined. The drought atlases and all of the DA and model products agree with each other on the positive PDSI responses over the western United States, central South America, the Mediterranean basin, and northern Russia, as well as the negative PDSI responses over European Russia, central Asia, and southern Siberia. Results from PHYDA show the strongest alignment with GEDA, NADAv2, and SADA (Fig. 7), while the PDSI responses from LMR v2.1 most closely match with those from ANZDA (Fig. 7). The spatial patterns of the PDSI responses from CESM1-LME agree better with MXDA than with the two DA products (Fig. 7), although the agreement across datasets is limited over the regions covered by ANZDA and SADA.

Next, Fig. 9 presents the global pattern of the persistence of PDSI responses to volcanic forcing from each dataset. As for SAT, persistence is defined as the number of years after the volcanic event for which the PDSI signal is significant at the 95% confidence level. The areas with PDSI persistence of more than 5 years are larger in the drought atlases, LMR v2.1, and PHYDA than in the CESM1-LME (Fig. 9). These results are mostly consistent with those of Tejedor et al. (2021b), with the key difference being that Tejedor et al. calculated

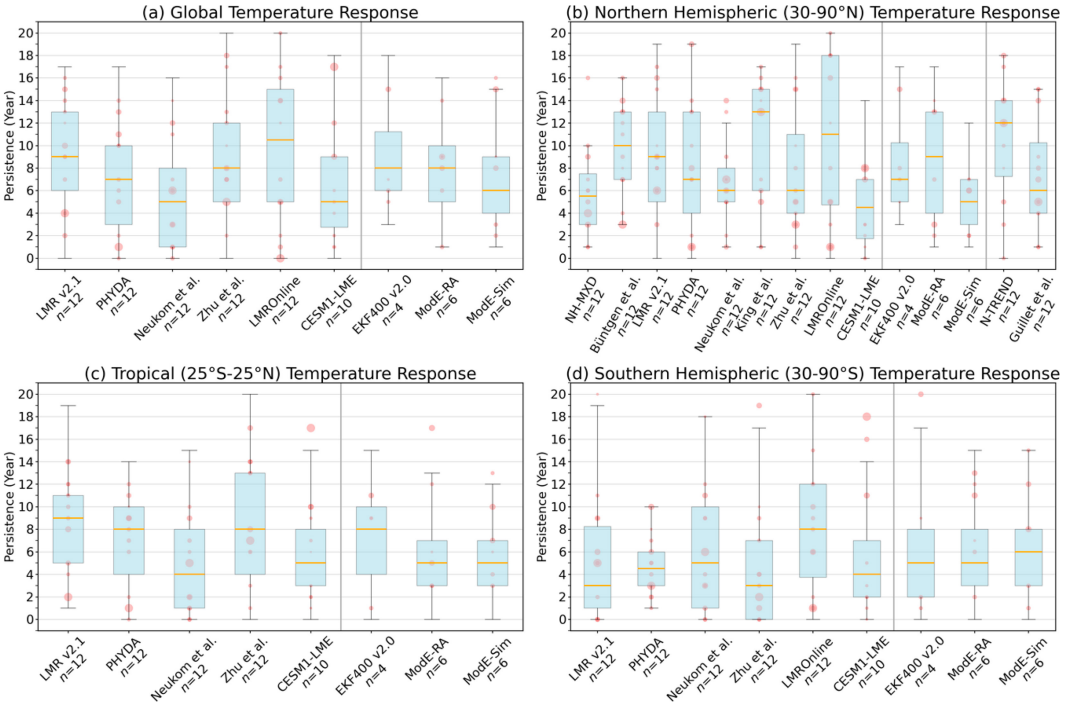

FIG. 6. The boxplots for the persistence of SAT responses to large tropical volcanic eruptions averaged over the (a) globe, (b) NH (30°–90°N), (c) tropics (25°S–25°N), and (d) SH (30°–90°S). The dots represent responses to individual volcanic events. The boxplots from the DA products and model simulations are based on all the ensemble members of the datasets, while the dots from the DA products and model simulations mark the ensemble means of the datasets. The sizes of the dots correspond to the intensities of the volcanic eruptions (i.e., a larger dot corresponds to a stronger volcanic eruption). Boxes range from the upper to the lower quartiles, whiskers indicate the 5th–95th percentiles, and the solid line is the median.

persistence using a weighted mean. As discussed in section 3a, the biological memory of tree rings might cause larger persistence in the tree-ring proxy and DA products compared to the model simulations, although it is unclear why the temperature persistence would be more in line with the model simulations as we have shown, while the PDSI persistence would disagree if the issue were solely caused by the influence of biological persistence. The clear mismatch between PDSI persistence in DA products and CESM1-LME contrasts with the closer agreement we find for SAT persistence (Fig. 6), indicating that the drivers of prolonged PDSI anomalies cannot be explained solely by biological memory in TRW proxies. Ocean–atmosphere feedbacks, such as ITCZ shifts, altered Walker circulation, or persistent SST anomalies, may amplify or sustain hydroclimate anomalies long after temperature returns to baseline. Land–atmosphere interactions, including soil moisture–vegetation feedbacks, could further reinforce these patterns. These processes together may explain why DA products and drought atlases systematically show longer-lived posteruption wet/dry anomalies than climate model ensembles. This mismatch highlights a key area for future work, particularly to disentangle proxy memory effects from dynamical feedbacks.

Finally, summer 500-hPa geopotential height composites (Fig. 10) show widespread negative anomalies, largest over the extratropical Northern Hemisphere, consistent with tropospheric cooling and column contraction. The relatively stronger midlatitude height reductions imply an enhanced meridional temperature gradient and a poleward displacement/strengthening of subtropical jets, together with extratropical wave train adjustments (Iles and Hegerl 2014; Zuo et al. 2019). These dynamical changes do not imply a uniform intensification of monsoon circulations. In many basins, reduced land–sea thermal contrast after eruptions weakens summer monsoon rainfall, and responses are regionally heterogeneous—including cases where the South American monsoon does not strengthen and can weaken. Accordingly, links to tropical PDSI are basin dependent: Some regions exhibit drying despite stronger jets aloft, while others show wetting, consistent with our reconstructed hydroclimate patterns. In fact, in Figs. 10a, 10d, and 10e, the 500-hPa geopotential height anomalies over northwestern North America and the extratropical North Atlantic are lower than those of the surroundings, which can induce westerly flow toward the western United States and toward the Mediterranean basin, thereby enhancing precipitation and the PDSI in these regions (Fig. 7).

4. Discussion

a. Temperature and hydroclimate impacts

Our synthesis confirms the robust near-global cooling that follows major tropical volcanic eruptions but also reveals

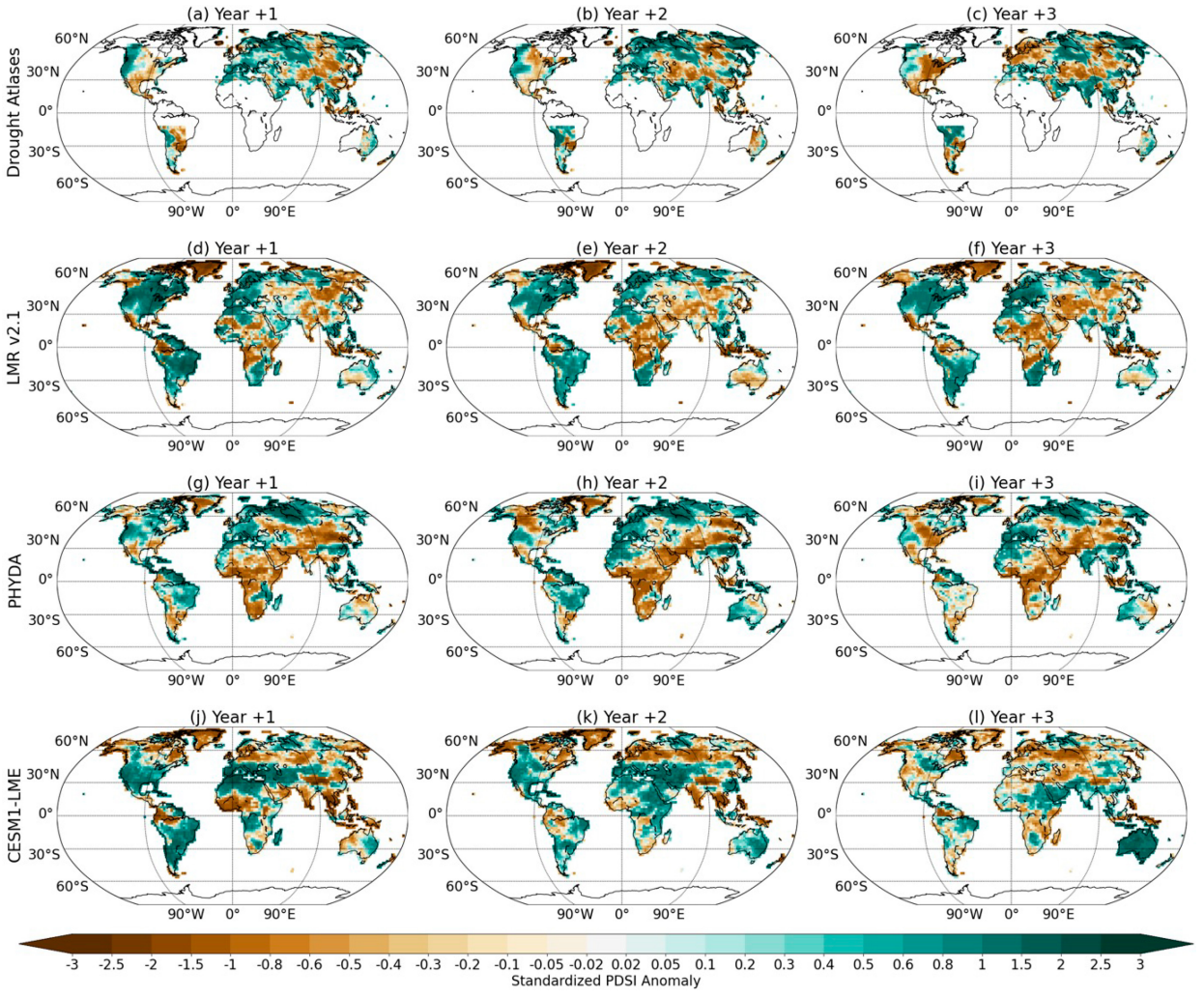

FIG. 7. The postvolcanic PDSI anomalies relative to the five pre-eruption years for the large tropical volcanic eruptions over the period 1500–1850 CE. The PDSI anomalies from the ANZDA, GEDA, MXDA, NADAv2, and SADA (a) 1, (b) 2, and (c) 3 years after the volcanic eruptions. (d)–(f) As in (a)–(c), but for LMR v2.1. (g)–(i) As in (a)–(c), but for PHYDA. (j)–(l) As in (a)–(c), but for CESM1-LME. The values from the drought atlases, PHYDA, and CESM1-LME represent summer PDSI anomalies. The values from LMR v2.1 represent annual PDSI anomalies. The results shown in (d)–(l) are based on the ensemble means of the datasets.

substantial differences in amplitude and persistence depending on reconstruction methodology. Reconstructions based on MXD (Schneider et al. 2017) reproduce cooling magnitudes and recovery times that are closely aligned with DA products and coupled model ensembles, suggesting that MXD provides a physically consistent benchmark for posteruption temperature evolution. In contrast, TRW-dominated reconstructions such as N-TREND and King et al. (2021) show comparable initial cooling but markedly longer persistence—often beyond 10 years—likely reflecting biological memory inherent to TRW chronologies (Lücke et al. 2019; Anchukaitis et al. 2017) rather than a prolonged radiative forcing.

A coherent cluster—NH-MXD (Schneider et al. 2017), offline DA products (e.g., LMR v2.1, PHYDA), and the CESM1-LME ensemble mean—shows posteruption SAT persistence of roughly 3–6 years, lending confidence that this time scale is physically plausible. LMROnline departs from this cluster with stronger and longer cooling, especially in the SH. We interpret this divergence as a methodological sensitivity, not as evidence that LMROnline is closer to truth. Two structural distinctions matter: (i) LMROnline is a single couple realization that retains slow internal modes and mixed-layer reemergence, whereas the CESM1-LME fields we compare are ensemble means that suppress such persistence; and (ii) online, coupled assimilation can advect and recirculate increments within the ocean–atmosphere system, potentially extending anomalies even after radiative forcing decays (Perkins and Hakim 2017; Tardif et al. 2019). This suggests that the longer LMROnline persistence likely reflects retained internal variability and assimilation methods rather than a systematically longer forced response. Resolving the discrepancy will require single member CESM comparisons,

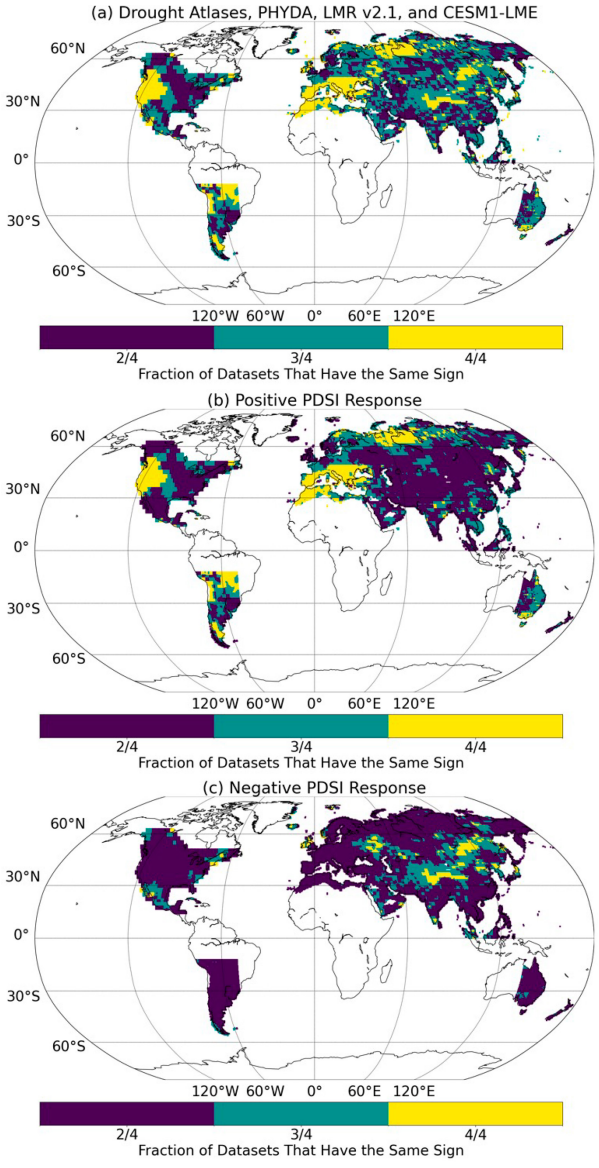

FIG. 8. The agreement in the signs of PDSI responses in Fig. 7 among the datasets. The agreement for (a) both positive and negative PDSI responses, (b) positive PDSI responses only, and (c) negative PDSI responses only.

LMROnline ensembles, and diagnostics of SH ocean heat storage/reemergence.

Although our results indicate that persistence is not strongly related to eruption stratospheric sulfur loading, this conclusion may partly reflect the influence of a few very large events. The 1257 Samalas eruption, despite its exceptional estimated VSSI (Vidal et al. 2016; Toohey and Sigl 2017), produces relatively muted cooling in several reconstructions—consistent with modeling results that show a weaker-than-expected temperature response for this event (Timmreck et al. 2009). Such discrepancies suggest that factors beyond stratospheric sulfate loading—such as eruption season, latitude, and the prevailing climate state—play an important role in shaping posteruption climate impacts. Future studies should perform sensitivity analyses excluding dominant eruptions like Samalas or stratifying events by season and latitude to better isolate the respective roles of external forcing, internal variability, and background climate conditions.

Hydroclimate responses are more spatially heterogeneous but reveal several robust patterns. Posteruption wetting is consistent over the western United States, the Mediterranean basin, and southern South America, whereas drying is observed across northern Eurasia, European Russia, central Asia, and southern Siberia. These signals are consistent with the Old World and Great Eurasian Drought Atlases (Cook et al. 2015, 2024) and with evidence for posteruption wetting in the Mediterranean region (Rao et al. 2017), suggesting that these responses are not artifacts of proxy network distribution, but instead reflect a physically coherent hydroclimate adjustment.

An important finding is that persistence of PDSI is distinctly different among CESM1-LME and DA products or drought atlases. While CESM exhibits rapid hydroclimate recovery within 1–3 years, there are certain DA products that maintain large anomalies for nearly a decade in certain regions. This discrepancy cannot be accounted for by TRW's biological persistence alone, as the PDSI is not an exclusively TRW-based index. Instead, it likely reflects the influence of other feedbacks, such as soil moisture, vegetation–climate interactions, and coupled ocean–atmosphere adjustments (e.g., ITCZ displacement, changes in Walker circulation) that are underrepresented or dampened in model-based ensemble means (Tejedor et al. 2021b).

ENSO responses following large tropical volcanic eruptions are generally weak and inconsistent across datasets. Even after the inclusion of coral proxies in all DA products, no statistically significant Niño-3.4 anomaly becomes apparent following eruptions, despite ensemble-mean filtering in CESM1-LME to suppress internal variability. This agrees with the results by Dee et al. (2020) and Zhu et al. (2022), who suggested that any tendency toward volcanically forced ENSO signals is small compared to internal variability and may be modulated by the prevailing ENSO phase at the time of eruption (Predybaylo et al. 2017). The lack of a uniform ENSO response lends strength to the interpretation that the hydroclimatic anomalies we detect reflect immediate responses to radiative forcing and to adjustments in circulation, rather than being systemically mediated by ENSO teleconnections. Additionally, the Niño-3.4 index is defined in our analysis as the absolute SAT or SST anomaly averaged over the equatorial central Pacific. It is worth noting that some studies, such as Khodri et al. (2017), employ a relative ENSO index that removes the tropical mean signal to better isolate the dynamic, El Niño–like component of the volcanic response. While the use of a relative index may more clearly reveal the atmospheric teleconnection, our finding of substantial disagreement across products, even with the absolute index, reinforces the conclusion that any volcanically forced signal is weak relative to internal variability, regardless of the precise index definition.

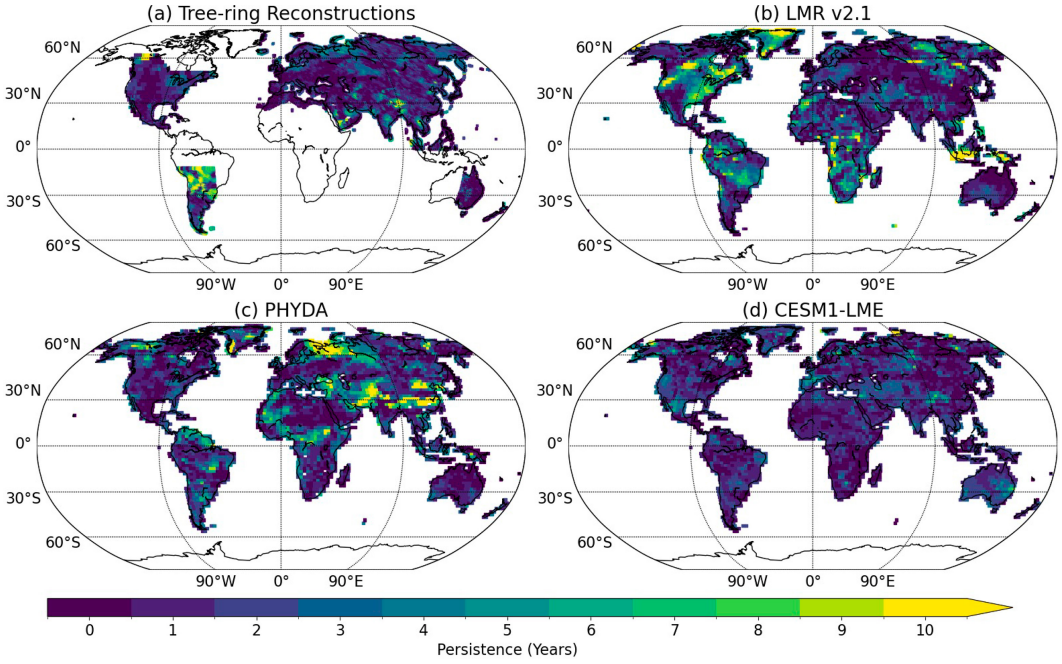

FIG. 9. The global patterns of the persistence of PDSI responses to large tropical volcanic eruptions from the (a) tree-ring-based drought atlases ANZDA, GEDA, MXDA, NADAv2, and SADA, (b) LMR v2.1, (c) PHYDA, and (d) CESM1-LME.

Finally, our analysis of 500-hPa geopotential height anomalies provides an important dynamical context. Widespread negative height anomalies are in agreement with the shrinkage of the posteruption troposphere, while extratropical SH wave trains indicate the reorganizing of extratropical flow. These circulation anomalies are consistent with the PDSI responses observed over regions of coherent hydroclimate signal and align with the poleward migration of the subtropical jet and altered storm-track behavior, as previously modeled (Iles and Hegerl 2014; Zuo et al. 2019).

b. *Uncertainties and future directions*

Although our synthesis reveals consistent large-scale signals, important uncertainties persist that limit a complete understanding of the link between volcanic forcing and climate.

First, hydroclimate reconstructions remain sparsely distributed, with large gaps over Africa, South Asia, and Oceania. The limited proxy coverage likely explains the low interproduct agreement in these regions. Expanding drought atlases into the tropics and Southern Hemisphere (Cook et al. 2024) and assimilating additional precipitation-sensitive proxies—such as speleothem $\delta^{18}O$, corals, and historical records—would significantly improve constraints on regional hydroclimate responses.

Second, a notable mismatch emerges between temperature persistence—where models, MXD reconstructions, and DA products broadly agree on a recovery time scale of 3–6 years—and PDSI persistence, which is considerably longer in DA products and drought atlases than in CESM1-LME. This suggests that the hydroclimate discrepancy is not simply an artifact of TRW biological memory but instead reflects additional processes—such as soil moisture memory, vegetation–climate coupling, or ocean–atmosphere feedbacks (e.g., ITCZ/Walker circulation shifts)—that may be underrepresented or damped in model ensemble means. Improving the representation of these feedbacks in models and DA systems should be a priority for future work.

Third, seasonal discrepancies among datasets may introduce ambiguity into amplitude estimates. Many tree-ring and DA products target JJA, and JJA fields were used in CESM-LME when available, but several datasets only provide annual means. While centering anomalies to the eruption year and using multiyear means reduces this sensitivity, stratifying results based on annual versus seasonally resolved datasets in future research can help avoid introducing potential biases, particularly at high latitudes, where winter and summer responses may vary significantly (Anchukaitis and Smerdon 2022; Tejedor et al. 2024).

Fourth, ENSO responses remain poorly constrained. Despite coral assimilation, DA products produce different Niño-3.4 responses. Denser, higher-resolution coral networks and other marine proxies (e.g., foraminifera Mg/Ca, alkenones) are needed to determine whether posteruption ENSO anomalies are forced or largely stochastic.

Finally, the lack of a direct scaling between stratospheric sulfur loading size and climate response remains an open problem. Some studies show that aerosol size distributions (Stoffel et al. 2024) and enhanced ocean–atmosphere latent heat flux during giant eruptions (Gao and Gao 2024) will partially offset radiative forcing. Detailed model simulations with improved aerosol microphysics and interactive ocean–atmosphere coupling are

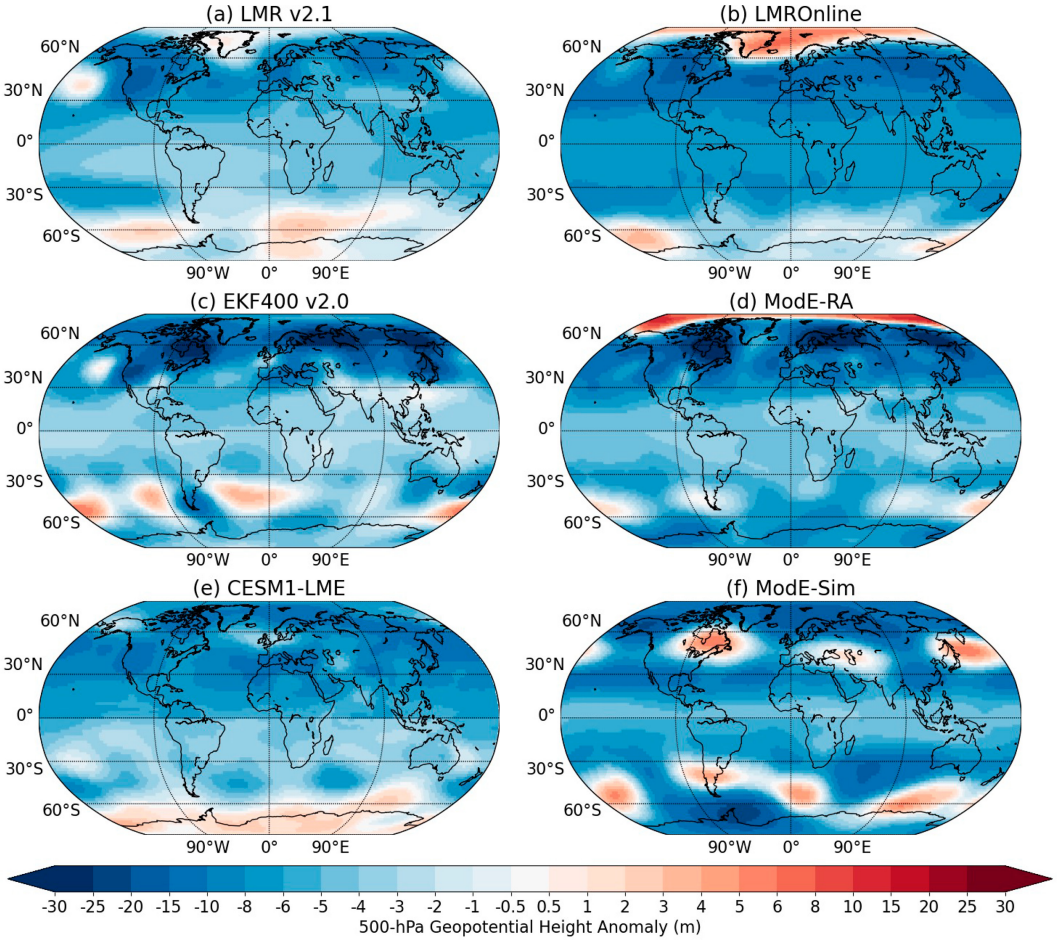

FIG. 10. The 3-yr averaged postvolcanic 500-hPa geopotential height anomalies relative to the five pre-eruption years for the large tropical volcanic eruptions over 1500–1850 CE. The 500-hPa geopotential height anomalies from the (a) LMR v2.1, (b) LMROnline, (c) EKF400 v2.0, (d) ModE-RA, (e) CESM1-LME, and (f) ModE-Sim. The values from LMR v2.1 and LMROnline represent annual height anomalies. The values from EKF400 v2.0, ModE-RA, CESM1-LME, and ModE-Sim represent summertime height anomalies (JJA in the NH and DJF height anomalies in the SH).

needed to explain why some of the largest eruptions of the last thousand years produced only moderate climate anomalies.

5. Conclusions

Our findings confirm that large tropical volcanic eruptions cause a clear and widespread cooling of global surface air temperatures. However, we also find substantial variation in both the magnitude and persistence of this cooling depending on the dataset used. Reconstructions based on MXD appear to give the most realistic estimate of the duration of posteruption cooling, while products dominated by TRW data and some data assimilation approaches tend to show cooling that lasts longer than expected. The hydroclimate response, as measured by PDSI, shows consistent wetting or drying in only a few regions, with much less agreement elsewhere. Importantly, no consistent ENSO response emerges across the datasets, even when averaging over large model ensembles to minimize internal variability. Finally, the geopotential height fields reveal broad tropospheric contraction and shifts in circulation that line up with the regions where hydroclimate responses are most coherent. Taken together, these results provide a framework for understanding how volcanic eruptions affect climate, highlight the influence of proxy network composition and assimilation methods on the reconstructed signals, and point to key regions—particularly in the tropics and the Southern Hemisphere—where additional high-resolution proxy records would help most to reduce current uncertainties.

Acknowledgments. We wish to dedicate this work to the memory of our first author, Dr. Zhaoxiangrui He, who sadly passed away during the review process. His dedication and scientific rigor were central to the conception, execution, and writing of this study. His commitment to advancing our understanding of past climate variability continues to inspire us. We extend our deepest condolences to his

family, friends, and colleagues, and we hope that this publication stands as a lasting tribute to his contributions. May he rest in peace. This study was supported by the U.S. National Science Foundation (OISE-1743738, AGS-2303352, AGS-2303353, AGS-2101214, and AGS-2127684). The authors appreciate the National Oceanic and Atmospheric Administration (NOAA) National Centers for Environmental Information (NCEI), the World Data Center for Climate (WDCC), and Zenodo for providing the data used in this study. ET received funding through the Comunidad de Madrid program Atracción Talento "César Nombela" (Grant 2023-T1/ECO-29118) and the MEDYRISK project (Grant PID2024-160542OB-I00) funded by MICIU/AEI/10.13039/501100011033 and ERDF/EU.

Data availability statement. All data used in this study are openly available online and can be downloaded using the links in Tables 1–3.

REFERENCES

Adams, J. B., M. E. Mann, and C. M. Ammann, 2003: Proxy evidence for an El Nino-like response to volcanic forcing. *Nature*, **426**, 274–278, https://doi.org/10.1038/nature02101.

Anchukaitis, K. J., and J. E. Smerdon, 2022: Progress and uncertainties in global and hemispheric temperature reconstructions of the Common Era. *Quat. Sci. Rev.*, **286**, 107537, https://doi.org/10.1016/j.quascirev.2022.107537.

——, and Coauthors, 2017: Last millennium Northern Hemisphere summer temperatures from tree rings: Part II, spatially resolved reconstructions. *Quat. Sci. Rev.*, **163**, 1–22, https://doi.org/10.1016/j.quascirev.2017.02.020.

Bhend, J., J. Franke, D. Folini, M. Wild, and S. Brönnimann, 2012: An ensemble-based approach to climate reconstructions. *Climate Past*, **8**, 963–976, https://doi.org/10.5194/cp-8-963-2012.

Briffa, K. R., P. D. Jones, F. H. Schweingruber, and T. J. Osborn, 1998: Influence of volcanic eruptions on Northern Hemisphere summer temperature over the past 600 years. *Nature*, **393**, 450–455, https://doi.org/10.1038/30943.

Büntgen, U., and Coauthors, 2021: The influence of decision-making in tree ring-based climate reconstructions. *Nat. Commun.*, **12**, 3411, https://doi.org/10.1038/s41467-021-23627-6.

Cheng, L., and Coauthors, 2022: Past and future ocean warming. *Nat. Rev. Earth Environ.*, **3**, 776–794, https://doi.org/10.1038/s43017-022-00345-1.

Colose, C. M., A. N. LeGrande, and M. Vuille, 2016: Hemispherically asymmetric volcanic forcing of tropical hydroclimate during the last millennium. *Earth Syst. Dyn.*, **7**, 681–696, https://doi.org/10.5194/esd-7-681-2016.

Cook, B. I., E. R. Cook, K. J. Anchukaitis, and D. Singh, 2024: Characterizing the 2010 Russian heat wave–Pakistan flood concurrent extreme over the last millennium using the Great Eurasian Drought Atlas. *J. Climate*, **37**, 4389–4401, https://doi.org/10.1175/JCLI-D-23-0773.1.

Cook, E. R., C. A. Woodhouse, C. M. Eakin, D. M. Meko, and D. W. Stahle, 2004: Long-term aridity changes in the western United States. *Science*, **306**, 1015–1018, https://doi.org/10.1126/science.1102586.

——, and Coauthors, 2015: Old world megadroughts and pluvials during the common era. *Sci. Adv.*, **1**, e1500561, https://doi.org/10.1126/sciadv.1500561.

D'Arrigo, R., R. Wilson, and K. J. Anchukaitis, 2013: Volcanic cooling signal in tree ring temperature records for the past millennium. *J. Geophys. Res. Atmos.*, **118**, 9000–9010, https://doi.org/10.1002/JGRD.50692.

D'Arrigo, R. D., G. C. Jacoby, and R. M. Free, 1992: Tree-ring width and maximum latewood density at the North American tree line: Parameters of climatic change. *Can. J. For. Res.*, **22**, 1290–1296, https://doi.org/10.1139/x92-171.

Dee, S. G., and N. J. Steiger, 2022: ENSO's response to volcanism in a data assimilation-based paleoclimate reconstruction over the Common Era. *Paleoceanogr. Paleoclimatol.*, **37**, e2021PA004290, https://doi.org/10.1029/2021PA004290.

——, K. M. Cobb, J. Emile-Geay, T. R. Ault, R. L. Edwards, H. Cheng, and C. D. Charles, 2020: No consistent ENSO response to volcanic forcing over the last millennium. *Science*, **367**, 1477–1481, https://doi.org/10.1126/science.aax2000.

Emile-Geay, J., R. Seager, M. A. Cane, E. R. Cook, and G. H. Haug, 2008: Volcanoes and ENSO over the past millennium. *J. Climate*, **21**, 3134–3148, https://doi.org/10.1175/2007JCLI1884.1.

Esper, J., L. Schneider, J. E. Smerdon, B. R. Schöne, and U. Büntgen, 2015: Signals and memory in tree-ring width and density data. *Dendrochronologia*, **35**, 62–70, https://doi.org/10.1016/j.dendro.2015.07.001.

Franke, J., V. Valler, Y. Brugnara, and S. Brönnimann, 2020: Ensemble Kalman Fitting Paleo-Reanalysis version 2 (EKF400_v2). World Data Center for Climate (WDCC) at DKRZ, accessed 19 September 2023, https://doi.org/10.26050/WDCC/EKF400_v2.0.

Gao, C. C., and Y. J. Gao, 2018: Revisited Asian monsoon hydroclimate response to volcanic eruptions. *J. Geophys. Res. Atmos.*, **123**, 7883–7896, https://doi.org/10.1029/2017JD027907.

Gao, C., A. Robock, and C. Ammann, 2008: Volcanic forcing of climate over the last 1500 years: An improved ice core-based index for climate models. *J. Geophys. Res.*, **113**, D23111, https://doi.org/10.1029/2008JD010239.

Gao, Y., and C. Gao, 2024: Dwindling effective radiative forcing of large volcanic eruption: The compensation role of ocean latent heat flux. *Geophys. Res. Lett.*, **51**, e2024GL109885, https://doi.org/10.1029/2024GL109885.

Giorgetta, M. A., and Coauthors, 2013: Climate and carbon cycle changes from 1850 to 2100 in MPI-ESM simulations for the Coupled Model Intercomparison Project phase 5. *J. Adv. Model. Earth Syst.*, **5**, 572–597, https://doi.org/10.1002/jame.20038.

Goosse, H., E. Crespin, A. de Montety, M. E. Mann, H. Renssen, and A. Timmermann, 2010: Reconstructing surface temperature changes over the past 600 years using climate model simulations with data assimilation. *J. Geophys. Res.*, **115**, D09108, https://doi.org/10.1029/2009JD012737.

Guillet, S., and Coauthors, 2017: Climate response to the Samalas volcanic eruption in 1257 revealed by proxy records. *Nat. Geosci.*, **10**, 123–128, https://doi.org/10.1038/ngeo2875.

Hegerl, G. C., T. J. Crowley, S. K. Baum, K.-Y. Kim, and W. T. Hyde, 2003: Detection of volcanic, solar and greenhouse gas signals in paleo-reconstructions of Northern Hemispheric temperature. *Geophys. Res. Lett.*, **30**, 1242, https://doi.org/10.1029/2002GL016635.

Iles, C. E., and G. C. Hegerl, 2014: The global precipitation response to volcanic eruptions in the CMIP5 models. *Environ.*

Res. Lett., **9**, 104012, https://doi.org/10.1088/1748-9326/9/10/104012.

IPCC, 2021: *Climate Change 2021: The Physical Science Basis.* V. Masson-Delmotte et al., Eds., Cambridge University Press, 2391 pp.

Jones, P. D., K. R. Briffa, and F. H. Schweingruber, 1995: Tree-ring evidence of the widespread effects of explosive volcanic eruptions. *Geophys. Res. Lett.*, **22**, 1333–1336, https://doi.org/10.1029/94GL03113.

Khodri, M., and Coauthors, 2017: Tropical explosive volcanic eruptions can trigger El Niño by cooling tropical Africa. *Nat. Commun.*, **8**, 778, https://doi.org/10.1038/s41467-017-00755-6.

King, J. M., K. J. Anchukaitis, J. E. Tierney, G. J. Hakim, J. Emile-Geay, F. Zhu, and R. Wilson, 2021: A data assimilation approach to last millennium temperature field reconstruction using a limited high-sensitivity proxy network. *J. Climate*, **34**, 7091–7111, https://doi.org/10.1175/JCLI-D-20-0661.1.

Lücke, L. J., G. C. Hegerl, A. P. Schurer, and R. Wilson, 2019: Effects of memory biases on variability of temperature reconstructions. *J. Climate*, **32**, 8713–8731, https://doi.org/10.1175/JCLI-D-19-0184.1.

Maher, N., S. McGregor, M. H. England, and A. S. Gupta, 2015: Effects of volcanism on tropical variability. *Geophys. Res. Lett.*, **42**, 6024–6033, https://doi.org/10.1002/2015GL064751.

Man, W., T. Zhou, and J. H. Jungclaus, 2014: Effects of large volcanic eruptions on global summer climate and East Asian monsoon changes during the last millennium: Analysis of MPI-ESM simulations. *J. Climate*, **27**, 7394–7409, https://doi.org/10.1175/JCLI-D-13-00739.1.

McGregor, S., A. Timmermann, and O. Timm, 2010: A unified proxy for ENSO and PDO variability since 1650. *Climate Past*, **6**, 1–17, https://doi.org/10.5194/cp-6-1-2010.

Morales, M. S., and Coauthors, 2020: Six hundred years of South American tree rings reveal an increase in severe hydroclimatic events since mid-20th century. *Proc. Natl. Acad. Sci. USA*, **117**, 16 816–16 823, https://doi.org/10.1073/pnas.2002411117.

Neukom, R., N. Steiger, J. J. Gómez-Navarro, J. Wang, and J. P. Werner, 2019: No evidence for globally coherent warm and cold periods over the preindustrial Common Era. *Nature*, **571**, 550–554, https://doi.org/10.1038/s41586-019-1401-2.

Ohba, M., H. Shiogama, T. Yokohata, and M. Watanabe, 2013: Impact of strong tropical volcanic eruptions on ENSO simulated in a coupled GCM. *J. Climate*, **26**, 5169–5182, https://doi.org/10.1175/JCLI-D-12-00471.1.

Otto-Bliesner, B. L., and Coauthors, 2016: Climate variability and change since 850 CE: An ensemble approach with the Community Earth System Model. *Bull. Amer. Meteor. Soc.*, **97**, 735–754, https://doi.org/10.1175/BAMS-D-14-00233.1.

Palmer, J. G., and Coauthors, 2015: Drought variability in the eastern Australia and New Zealand summer drought atlas (ANZDA, CE 1500–2012) modulated by the Interdecadal Pacific Oscillation. *Environ. Res. Lett.*, **10**, 124002, https://doi.org/10.1088/1748-9326/10/12/124002.

Pausata, F. S. R., L. Chafik, R. Caballeroa, and D. S. Battisti, 2015: Impacts of high-latitude volcanic eruptions on ENSO and AMOC. *Proc. Natl. Acad. Sci. USA*, **112**, 13 784–13 788, https://doi.org/10.1073/pnas.1509153112.

Perkins, W. A., and G. J. Hakim, 2017: Reconstructing paleoclimate fields using online data assimilation with a linear inverse model. *Climate Past*, **13**, 421–436, https://doi.org/10.5194/cp-13-421-2017.

Predybaylo, E., G. L. Stenchikov, A. T. Wittenberg, and F. Zeng, 2017: Impacts of a Pinatubo-size volcanic eruption on ENSO. *J. Geophys. Res. Atmos.*, **122**, 925–947, https://doi.org/10.1002/2016JD025796.

Rao, M. P., and Coauthors, 2017: European and Mediterranean hydroclimate responses to tropical volcanic forcing over the last millennium. *Geophys. Res. Lett.*, **44**, 5104–5112, https://doi.org/10.1002/2017GL073057.

Samakinwa, E., V. Valler, R. Hand, R. Neukom, J. J. Gómez-Navarro, J. Kennedy, N. A. Rayner, and S. Brönnimann, 2021: An ensemble reconstruction of global monthly sea surface temperature and sea ice concentration 1000–1849. *Sci. Data*, **8**, 261, https://doi.org/10.1038/s41597-021-01043-1.

Schneider, L., J. E. Smerdon, U. Büntgen, R. J. S. Wilson, V. S. Myglan, A. V. Kirdyanov, and J. Esper, 2015: Revising mid-latitude summer temperatures back to A.D. 600 based on a wood density network. *Geophys. Res. Lett.*, **42**, 4556–4562, https://doi.org/10.1002/2015GL063956.

——, ——, F. Pretis, C. Hartl-Meier, and J. Esper, 2017: A new archive of large volcanic events over the past millennium derived from reconstructed summer temperatures. *Environ. Res. Lett.*, **12**, 094005, https://doi.org/10.1088/1748-9326/aa7a1b; Corrigendum, **12**, 119501, https://doi.org/10.1088/1748-9326/aa9426.

Smerdon, J. E., E. R. Cook, and N. J. Steiger, 2023: The historical development of large-scale paleoclimate field reconstructions over the Common Era. *Rev. Geophys.*, **61**, e2022RG000782, https://doi.org/10.1029/2022RG000782.

Stahle, D. W., and Coauthors, 2016: The Mexican Drought Atlas: Tree-ring reconstructions of the soil moisture balance during the late pre-Hispanic, colonial, and modern eras. *Quat. Sci. Rev.*, **149**, 34–60, https://doi.org/10.1016/j.quascirev.2016.06.018.

Steiger, N., J. E. Smerdon, E. R. Cook, and B. I. Cook, 2018: A reconstruction of global hydroclimate and dynamical variables over the Common Era. *Sci. Data*, **5**, 180086, https://doi.org/10.1038/sdata.2018.86.

Stenchikov, G., T. L. Delworth, V. Ramaswamy, R. J. Stouffer, A. Wittenberg, and F. Zeng, 2009: Volcanic signals in oceans. *J. Geophys. Res.*, **114**, D16104, https://doi.org/10.1029/2008JD011673.

Stevenson, S., B. Otto-Bliesner, J. Fasullo, and E. Brady, 2016: "El Niño like" hydroclimate responses to last millennium volcanic eruptions. *J. Climate*, **29**, 2907–2921, https://doi.org/10.1175/JCLI-D-15-0239.1.

Stoffel, M., and Coauthors, 2015: Estimates of volcanic-induced cooling in the Northern Hemisphere over the past 1,500 years. *Nat. Geosci.*, **8**, 784–788, https://doi.org/10.1038/ngeo2526.

——, C. Corona, and S. St. George, 2024: The next massive volcano eruption will cause climate chaos–and we are unprepared. *Nature*, **635**, 286–289, https://doi.org/10.1038/d41586-024-03680-z.

Tardif, R., and Coauthors, 2019: Last Millennium Reanalysis with an expanded proxy database and seasonal proxy modeling. *Climate Past*, **15**, 1251–1273, https://doi.org/10.5194/cp-15-1251-2019.

Tejedor, E., N. Steiger, J. E. Smerdon, R. Serrano-Notivoli, and M. Vuille, 2021a: Global temperature responses to large tropical volcanic eruptions in paleo data assimilation products and climate model simulations over the Last Millennium. *Paleoceanogr. Paleoclimatol.*, **36**, e2020PA004128, https://doi.org/10.1029/2020PA004128.

——, N. J. Steiger, J. E. Smerdon, R. Serrano-Notivoli, and M. Vuille, 2021b: Global hydroclimatic response to tropical volcanic eruptions over the last millennium. *Proc. Natl. Acad. Sci. USA*, **118**, e2019145118, https://doi.org/10.1073/pnas.2019145118.

——, L. M. Polvani, N. J. Steiger, M. Vuille, and J. E. Smerdon, 2024: No evidence of winter warming in Eurasia following large, low-latitude volcanic eruptions during the last millennium. *J. Climate*, **37**, 5653–5673, https://doi.org/10.1175/JCLI-D-23-0625.1.

Timmreck, C., S. J. Lorenz, T. J. Crowley, S. Kinne, T. J. Raddatz, M. A. Thomas, and J. H. Jungclaus, 2009: Limited temperature response to the very large AD 1258 volcanic eruption. *Geophys. Res. Lett.*, **36**, L21708, https://doi.org/10.1029/2009GL040083.

Toohey, M., and M. Sigl, 2017: Volcanic stratospheric sulfur injections and aerosol optical depth from 500 BCE to 1900 CE. *Earth Syst. Sci. Data*, **9**, 809–831, https://doi.org/10.5194/essd-9-809-2017.

——, and ——, 2019: Reconstructed volcanic stratospheric sulfur injections and aerosol optical depth, 500 BCE to 1900 CE, version 3. World Data Center for Climate (WDCC) at DKRZ, accessed 6 December 2023, https://doi.org/10.26050/WDCC/eVolv2k_v3.

Valler, V., J. Franke, Y. Brugnara, and S. Brönnimann, 2022: An updated global atmospheric paleo-reanalysis covering the last 400 years. *Geosci. Data J.*, **9**, 89–107, https://doi.org/10.1002/gdj3.121.

——, and Coauthors, 2023: ModE-RA–A global monthly paleo-reanalysis of the modern era (1421 to 2008): Set 1420-3_1850-1. World Data Center for Climate (WDCC) at DKRZ, accessed 24 February 2024, https://doi.org/10.26050/WDCC/ModE-RA_s14203-18501.

——, and Coauthors, 2024: ModE-RA: A global monthly paleo-reanalysis of the modern era 1421 to 2008. *Sci. Data*, **11**, 36, https://doi.org/10.1038/s41597-023-02733-8.

van der Schrier, G., and J. Barkmeijer, 2005: Bjerknes' hypothesis on the coldness during AD 1790–1820 revisited. *Climate Dyn.*, **24**, 355–371, https://doi.org/10.1007/s00382-004-0506-x.

Vidal, C. M., and Coauthors, 2016: The 1257 Samalas eruption (Lombok, Indonesia): The single greatest stratospheric gas release of the Common Era. *Sci. Rep.*, **6**, 34868, https://doi.org/10.1038/srep34868.

Villamayor, J., M. Khodri, S.-W. Fang, J. H. Jungclaus, C. Timmreck, and D. Zanchettin, 2023: Sahel droughts induced by large volcanic eruptions over the last millennium in PMIP4/Past1000 simulations. *Geophys. Res. Lett.*, **50**, e2022GL101478, https://doi.org/10.1029/2022GL101478.

Wahl, E. R., H. F. Diaz, J. E. Smerdon, and C. M. Ammann, 2014: Late winter temperature response to large tropical volcanic eruptions in temperate western North America: Relationship to ENSO phases. *Global Planet. Change*, **122**, 238–250, https://doi.org/10.1016/j.gloplacha.2014.08.005.

Whitaker, J. S., and T. M. Hamill, 2002: Ensemble data assimilation without perturbed observations. *Mon. Wea. Rev.*, **130**, 1913–1924, https://doi.org/10.1175/1520-0493(2002)130<1913:EDAWPO>2.0.CO;2.

Wilson, R., and Coauthors, 2016: Last millennium Northern Hemisphere summer temperatures from tree rings: Part I: The long term context. *Quat. Sci. Rev.*, **134**, 1–18, https://doi.org/10.1016/j.quascirev.2015.12.005.

Zanchettin, D., O. Bothe, H. F. Graf, S. J. Lorenz, J. Luterbacher, C. Timmreck, and J. H. Jungclaus, 2013: Background conditions influence the decadal climate response to strong volcanic eruptions. *J. Geophys. Res. Atmos.*, **118**, 4090–4106, https://doi.org/10.1002/jgrd.50229.

——, and Coauthors, 2016: The Model Intercomparison Project on the climatic response to Volcanic forcing (VolMIP): Experimental design and forcing input data for CMIP6. *Geosci. Model Dev.*, **9**, 2701–2719, https://doi.org/10.5194/gmd-9-2701-2016.

Zhou, S., F. Liu, A. Dai, and T. Zhao, 2024: Dryland hydroclimatic response to large tropical volcanic eruptions during the last millennium. *npj Climate Atmos. Sci.*, **7**, 85, https://doi.org/10.1038/s41612-024-00636-y.

Zhu, F., J. Emile-Geay, G. J. Hakim, J. King, and K. J. Anchukaitis, 2020: Resolving the differences in the simulated and reconstructed temperature response to volcanism. *Geophys. Res. Lett.*, **47**, e2019GL086908, https://doi.org/10.1029/2019GL086908.

——, ——, K. J. Anchukaitis, G. J. Hakim, A. T. Wittenberg, M. S. Morales, M. Toohey, and J. King, 2022: A re-appraisal of the ENSO response to volcanism with paleoclimate data assimilation. *Nat. Commun.*, **13**, 747, https://doi.org/10.1038/s41467-022-28210-1.

Zuo, M., T. Zhou, and W. Man, 2019: Hydroclimate responses over global monsoon regions following volcanic eruptions at different latitudes. *J. Climate*, **32**, 4367–4385, https://doi.org/10.1175/JCLI-D-18-0707.1.